1   **Structure-based analysis of CysZ-mediated cellular uptake of sulfate**

2

3   **Authors and Affiliations:**

4   Zahra Assur Sanghai[1,2], Qun Liu[3], Oliver B. Clarke[2], Edgar Leal Pinto[4], Brian Kloss[5], Shantelle

5   Tabuso[5], James Love[5], Marco Punta[6], Surajit Banerjee[7], Kanagalaghatta R. Rajashankar[7],

6   Burkhard Rost[8], Diomedes Logothetis[4], Matthias Quick[9], Wayne A. Hendrickson[1,2,6] and Filippo

7   Mancia[1*]

8

9   [1] Department of Physiology and Cellular Biophysics, [2] Department of Biochemistry and

10   Molecular Biophysics, and [9] Department of Psychiatry, Center for Molecular Recognition,

11   Columbia University, New York, NY 10032, USA.

12   [3] Biology Department, Brookhaven National Laboratory, Upton, NY 11973, USA.

13   [4] Department of Physiology and Biophysics, Virginia Commonwealth University School of

14   Medicine, Richmond, VA 23298, USA.

15   [5] New York Structural Biology Center, New York, NY 10027, USA.

16   [6] Centre for Evolution and Cancer, The Institute of Cancer Research, London, UK.

17   [7] Department of Chemistry and Chemical Biology, Cornell University, NE-CAT, Advanced

18   Photon Source, Argonne, IL 60439, USA.

19   [8] Department of Informatics, Technical University of Munich, Munich 85748, Germany

20

21   * To whom correspondence should be addressed: E-mail fm123@cumc.columbia.edu (F.M.)

22

23   **ABSTRACT**

24   **Sulfur, most abundantly found in the environment as sulfate (SO_4^{2-}), is an essential element**

25   **in metabolites required by all living cells, including amino acids, co-factors and vitamins.**

26   **Current understanding of the cellular delivery of SO_4^{2-} at the molecular level is limited**

27   **however. CysZ has been described as a SO_4^{2-} permease, but its sequence family is without**

28   **known structural precedent. Based on crystallographic structure information, SO_4^{2-}**

29   **binding and uptake experiments in cells and proteoliposomes, and single-channel**

30   **conductance measurements, we provide insight into the molecular mechanism of CysZ-**

31   **mediated translocation of SO_4^{2-} across membranes. CysZ properties differ markedly from**

32   **those of known transporters and ion channels. The structures display a hitherto unknown**

33   **fold with dual topology, assembling in CysZ from *Pseudomonas denitrificans* as a trimer of**

34   **antiparallel dimers in the membrane. CysZ structures from two other species recapitulate**

35   **dimers from this assembly. Mutational studies highlight the functional relevance of**

36   **conserved CysZ residues.**

37

38   Sulfur has a central role in many cellular processes across all kingdoms of life. It is a vital

39   component of several essential compounds, including the sulfur-containing amino acids cysteine

40   and methionine, in prosthetic groups such as the Fe-S clusters, as well as vitamins and

41   micronutrients such as biotin (vitamin H), thiamine (vitamin B1) and lipoic acid, and in

42   coenzymes A and M (Barton, 2005). Whilst mammals obtain the majority of the necessary

43   sulfur-containing metabolites directly from the diet, plants, fungi, and bacteria are able to

44   assimilate and utilize sulfur from organic and inorganic sources (Barton, 2005). Sulfate (SO_4^{2-}) is

45   the most abundant source of sulfur in the environment and its utilization is contingent upon its

2

46   entry into the cell (Kertesz, 2000). In certain fungi, and prokaryotes, once internalized, SO_4^{2-} is

47   first reduced to sulfite (SO_3^{2-}), and then further to sulfide (S^{2-}), a form that can be used by the

48   cell (Kredich, Hulanicka, & Hallquist, 1979) (Fig. 1-S1). In *Escherichia coli* and other gram-

49   negative bacteria, the culmination of the aforementioned sulfate assimilatory (also known as

50   reductive) pathway is the formation of cysteine by the addition of S^{2-} to O-acetylserine by

51   cysteine synthase, followed by the synthesis of methionine from homocysteine (Kredich, 1971)

52   (Fig. 1-S1).

53

54   In prokaryotes, the entry of SO_4^{2-} into the cell is mediated by four known families of dedicated

55   transport systems: the ABC sulfate transporter complexes SulT or CysTWA, the SulP family of

56   putative SLC13 sodium:sulfate or proton:sulfate symporters or SLC26 solute:sulfate exchangers,

57   the phosphate transporter-like CysP/PitA family, and the CysZ family classified as SO_4^{2-}

58   permeases (Aguilar-Barajas, Diaz-Perez, Ramirez-Diaz, Riveros-Rosas, & Cervantes, 2011;

59   Hryniewicz, Sirko, Palucha, Bock, & Hulanicka, 1990; Kertesz, 2001; Loughlin, Shelden,

60   Tierney, & Howitt, 2002; Mansilla & de Mendoza, 2000; Sirko, Zatyka, Sadowy, & Hulanicka,

61   1995). CysZ family members are 28-30 kDa bacterial inner-membrane proteins found

62   exclusively in prokaryotes with no apparent homology to any of the established channel or

63   transporter folds, and are scarcely studied in the literature (Zhang, Jiang, Nan, Almqvist, &

64   Huang, 2014). The *cysZ* gene owes its name to its presence in the cysteine biosynthesis regulon.

65   In two reports from thirty years ago, an *E. coli* K12 strain with a *cysZ* deletion showed a severe

66   impairment in its ability to accumulate SO_4^{2-} and was not viable in sulfate-free media without an

67   alternate sulfur source such as thiosulfate ($S_2O_3^{2-}$) (Britton et al., 1983; Parra, Britton, Castle,

68   Jones-Mortimer, & Kornberg, 1983). Recently, a third report studying the functional properties

69   of CysZ, concluded that the protein from *E. coli* functions as a high affinity, highly specific pH-

70   dependent SO_4^{2-} transporter, directly regulated by the toxic, assimilatory pathway intermediate,

71   SO_3^{2-} (Zhang et al., 2014).

72

73   To investigate the role of CysZ in cellular sulfate uptake at a molecular level, we have

74   undertaken an approach that combines structural and functional studies. To this end, we

75   determined the crystal structures of CysZ from three species, *Idiomarina loihiensis (Il; IlCysZ)*,

76   *Pseudomonas fragi (Pf; PfCysZ),* and *Pseudomonas denitrificans (Pd; PdCysZ)*, and

77   characterized CysZ function in purified form, in reconstituted proteoliposomes, in planar lipid

78   bilayers, and in cells. Combining the structural information from the three orthologs reveals that

79   CysZ features a novel protein fold that assembles as oligomers with a dual topology. This

80   arrangement can be understood as being derived from trimers of dimers akin to the hexameric

81   assembly captured in one of the structures. Interpreting the functional data in a structural context

82   has allowed us to formulate a mechanistic model for CysZ-mediated SO_4^{2-} translocation across

83   the bacterial cytoplasm membrane.

84

85   Both the structures and the functional properties of CysZ proteins are distinct from those of any

86   known membrane transporter or ion channel. Besides not resembling other transporter structures,

87   CysZ mediates sulfate uptake into cells or proteoliposomes without coupling to ion gradients,

88   partner proteins, or exogenous energy sources such as ATP. Besides differing from other ion

89   channel structures, CysZ generates sulfate currents across lipid bilayers with unusual

90   characteristics.   These distinctive properties make CysZ appealing as a model system for studies

91   of biophysical principles of membrane protein biogenesis and transmembrane ion passage.

92

RESULTS

Structure determination of CysZ

Following a structural genomics approach aimed at crystallization for structural analysis, we cloned and screened a total of 63 different bacterial homologs of CysZ for high-level expression and stability in detergents (Love et al., 2010; Mancia & Love, 2011). Crystal structures were determined for CysZ from three organisms. Chronologically, the structure of *Il*CysZ was the first solved, to 2.3 Å resolution in space group *C2* by SAD, initially based on a single selenate ion bound to the protein and subsequently also by selenomethione derivatization (SeMet) SAD, and multi-crystal native SAD (Liu et al., 2012). The structure of *Pf*CysZ was solved second, to 3.5 Å resolution, with crystals also belonging to space group *C2*. Although *Pf*CysZ and *Il*CysZ share 42% sequence identity, molecular replacement failed to find a convincing solution, and we instead used SeMet-derivatized *Pf*CysZ to obtain phase information by multi-crystal SeMet SAD. Third, we determined the structure of *Pd*CysZ, which crystallized in multiple forms belonging to space groups $P6_3$, $P4_122$ and $P2_12_12_1$, revealing the same architecture and oligomeric assembly each time (Fig. 1-S2b). *Pd*CysZ structures in the $P6_3$ and $P2_12_12_1$ lattices each contain an entire hexamer in their asymmetric units, whereas a molecular diad coincides with a crystallographic axis in the $P4_122$ lattice. We focused our analysis on the best of these (3.4 Å resolution in $P6_3$). The location of the selenium sites was obtained from a SeMet SAD data set, and the structure was solved by combining the resulting SAD phases with those from a molecular replacement solution obtained by positioning the *Pf*CysZ model (75% sequence identity) onto SeMet fiducials in the initial electron density map (Table 1, Fig. 1-S2a).

114

The hexameric structure of *Pd*CysZ

The refined structure of *Pd*CysZ comprises an entire hexamer of near-perfect D3 symmetry. Antiparallel pairs of protomers arrange together as a trimer of dimers (Fig. 1a), with the three-fold axis oriented perpendicular to the plane of the putative membrane and three two-fold axes between dimers of the hexamer. Both the periplasmic and cytoplasmic faces of the hexamer are essentially identical by symmetry, resulting in a dual-topology assembly for *Pd*CysZ. The hexamer has a triangular face of equal sides measuring approximately 75 Å, with the perpendicular span of about 65 Å. The interaction of the six protomers results in a total buried surface area (Krissinel & Henrick, 2007) of 5,700 Å^2. A surface electrostatic representation reveals a hydrophobic belt along the mid-section of the hexamer when viewed from its side, outlining the orientation of CysZ in the lipid bilayer (Czodrowski, Dramburg, Sotriffer, & Klebe, 2006; Dolinsky et al., 2007; Dolinsky, Nielsen, McCammon, & Baker, 2004) (Fig. 1b). A surface representation of the sequence conservation, calculated by analysis of multiple sequence alignments (MSA) (Ashkenazy et al., 2016; Glaser et al., 2003) highlights the regions of invariance in the sequence and in turn, the areas on the molecule that are most likely to have structural and functional importance (Fig. 1c).

The CysZ protomer is an alpha-helical integral membrane protein with two long transmembrane (TM) helices (H2b and H3a) and two pairs of shorter helices (H4b-H5a and H7-H8) that insert only partially into the membrane (hemi-penetrating), forming a funnel or tripod-like shape within the membrane (Fig. 2a, b). The protein has an extra-membranous hydrophilic 'head', comprising an iris-like arrangement of the two short helices, H1 and H6, and kinked helices H3b, H4a, and H5b. The amino and carboxyl termini are also located in this region (Fig. 2a, b). H4b and H5a lie

138   partly inserted in the membrane, with the turn between the two helices pointing in towards the

139   three-fold axis at the center of the hexamer. CysZ amino-acid sequences from different

140   organisms are very similar; for example, those of *Pd*CysZ and *E. coli* CysZ (*Ec*CysZ) are 40.5%

141   identical and those of *Ec*CysZ and our three structures have 30.0% of their residues exactly in

142   common (Fig. 2c). Helix boundaries are also essentially the same in the structures of *Pd*CysZ,

143   *Il*CysZ and *Pf*CysZ (Fig. 2c).

144

145   **The dimeric assembly of *Il*CysZ and *Pf*CysZ**

146   Unlike *Pd*CysZ, both *Il*CysZ and *Pf*CysZ crystallize as dimers (Fig. 3a, b), in agreement with

147   their different behavior in detergent-containing solution. Indeed, size-exclusion chromatography

148   runs of the three species of CysZ in the same buffer and detergent conditions, show mono-

149   disperse peaks eluting at 13.42 ml (*Il*CysZ), 13.95 ml (*Pf*CysZ) and 12.56 ml (*Pd*CysZ) (Fig. 3-

150   S1). This result is consistent with a different and smaller oligomeric state of *Il*CysZ and *Pf*CysZ

151   (similar retention volume) compared to *Pd*CysZ (eluting 1 ml ahead).

152

153   The protomers of the *Il*CysZ dimer are arranged in a head-to-tail antiparallel association, with

154   H4b-H5a protruding at an angle that is nearly parallel to the putative plane of the membrane

155   (Fig. 3a, 3-S2a, b). The *Pf*CysZ dimer is also arranged in an antiparallel orientation but with a

156   different dimer interface (Fig. 3b). In the *Pf*CysZ structure, H4b-H5a together form a narrower

157   angle with H2 and H3, and tuck-in closer to the rest of the molecule (Fig. 3b). The resulting

158   dumbbell-shaped *Pf*CysZ dimer is predicted, by OPM/PPM (Orientation of Proteins in

159   Membranes) (Lomize, Pogozheva, Joo, Mosberg, & Lomize, 2012), to lie in the membrane at a

160   31° tilt to the perpendicular, in agreement with the position of its central hydrophobic belt, as

161   revealed by surface-electrostatics calculations (Fig. 3- S2e, f). The dimer interfaces of *Il*CysZ and

162   *Pf*CysZ bury 780 Å^2 and 1136 Å^2 of surface area respectively (Krissinel & Henrick, 2007)

163

164   The individual protomers of CysZ from all three species adopt the same topology and fold, and

165   superpose well with an overall pairwise root mean squared deviation (r.m.s.d) of ~2.5 Å (Fig.

166   3c). The greatest variation between the protomers of each structure is seen in the orientation of

167   H4b-H5a with respect to the TM helices, H2 and H3 (Fig. 3c), which seem to be the most

168   conformationally flexible with respect to the rest of the molecule.

169

170   Comparison of the structures of *Il*CysZ and *Pf*CysZ with that of *Pd*CysZ revealed that these two

171   distinctive dimeric structures are both represented in the hexameric one. Indeed, the *Il*CysZ

172   dimer (Fig. 3a) resembles the vertically arranged pair of protomers in the *Pd*CysZ hexamer (Fig.

173   3d) at each of the vertices of the triangular structure. On the other hand, the *Pf*CysZ dimer (Fig.

174   3b) resembles the transverse pair of protomers lying at a tilt, just as was predicted by OPM

175   (Lomize et al., 2012), along the side of the *Pd*CysZ hexamer when viewed from inside the plane

176   of the membrane (Fig. 3e). In essence, the *Pd*CysZ hexamer can be seen as a trimer of either

177   *Il*CysZ or *Pf*CysZ dimers (Fig. 3f).

178

179   **Dual-topology assembly of CysZ**

180   To validate the dual-topology assembly of CysZ observed in all our structures, we performed

181   disulfide crosslinking assays on engineered cysteine mutants of CysZ designed to capture the

182   antiparallel dimer, utilizing isolated membranes. Disulfide-trapping experiments of the

183   transverse dimer, performed by crosslinking a pair of mutants (L161C-A164C) on H5 of *Pf*CysZ,

184   as well as the corresponding pair in *Il*CysZ (V157C-Q163C) confirm the dimer interface

185   observed in the structures of *Pf*CysZ and *Il*CysZ, and, as a consequence, the dual-topology

186   assembly of the two proteins (Fig. 3-S2f, g, h).

187

188   To further validate the dual-topology orientation of CysZ in the membrane, we performed a

189   cysteine accessibility scan experiment, mapping residues expected to be located outside the lipid

190   bilayer, by fluorescence labeling of the thiol groups of various single cysteine mutants with a

191   membrane-impermeable dye. Membrane fractions isolated from recombinant cultures expressing

192   *Il*CysZ cysteine mutants introduced at positions along the edge of helix H4 predicted to be

193   solvent accessible based on our structure, were indeed labeled with a membrane-impermeable

194   fluorescent thiol-specific maleimide dye (Fig. 3-S2c, d).

195

196   **Functional characterization of CysZ**

197   To characterize the functional properties of CysZ, we used a four-pronged approach: (i)

198   radiolabeled $[^{35}S]O_4^{2-}$ uptake experiments in cells expressing plasmid-encoded CysZ, (ii)

199   radiolabeled ($[^{35}S]O_4^{2-}$) binding to purified CysZ in detergent solution, (iii) $[^{35}S]O_4^{2-}$ uptake in

200   proteoliposomes reconstituted with purified CysZ, and (iv) single-channel electrophysiological

201   recordings in a planar lipid bilayer reconstituted with CysZ.

202   First, we compared the time course of SO_4^{2-} accumulation in an *E. coli cysZ* knockout strain (*E.*

203   *coli* K12 JW2406-1, CysZ⁻) (Baba et al., 2006) with that in the wild-type (WT, *E. coli* K12

204   BW25113, *cysZ⁺*) strain. CysZ⁻ cells, after growth in minimal media and 12 hours of sulfate

205   starvation, showed significantly diminished SO_4^{2-} uptake when compared to the WT strain,

206   consistent with previous results (Fig. 4a) (Parra et al., 1983). The CysZ⁻ strain still showed a low

207   level of sulfate accumulation, which could be attributed to the other endogenous sulfate transport

208   systems present in the bacteria (for example ABC transporter and SulP). This uptake-deficient

209   phenotype of the CysZ$^-$ cells could be rescued by plasmid-driven expression of PdCysZ (Fig.

210   4b), as well as IlCysZ and PfCysZ (data not shown). Consistent with previously reported data

211   (Zhang et al., 2014), we observed that SO_3^{2-} ions severely impede or block the accumulation of

212    $[^{35}S]O_4^{2-}$ by CysZ-expressing cells (Fig. 4b).

213

214   To further characterize the interaction of CysZ with both SO_4^{2-} and SO_3^{2-}, we performed binding

215   experiments on purified PdCysZ using the scintillation proximity assay (SPA) (Quick & Javitch,

216   2007). To determine the concentration of half-maximal binding (EC_{50}), we isotopically diluted

217    $[^{35}S]O_4^{2-}$ with non-labeled SO_4^{2-}, obtaining an EC_{50} of 0.81 ± 0.045 µM (Fig. 4c). Competing

218   binding of $[^{35}S]O_4^{2-}$ with SO_3^{2-} revealed that PdCysZ binds SO_3^{2-} with greater affinity as reflected

219   by a half-maximum inhibition constant (IC_{50}) of 0.12 ± 0.034 µM.

220

221   Next, we conducted $[^{35}S]O_4^{2-}$ uptake experiments on detergent solubilized and purified CysZ

222   reconstituted in proteoliposomes. Proteoliposomes provide a means for assessing the activity of a

223   membrane protein independent of other proteins found natively in cellular expression systems.

224   Such binding partners could be involved in SO_4^{2-} uptake as measured in intact $E.\ coli$ cells (Fig.

225   4a). Furthermore, in addition to the SPA measurements, these experiments allowed us to confirm

226   that the detergent-based extraction from the membrane and purification of CysZ used for our

227   crystallization approaches did not compromise its activity. Acting alone, PdCysZ in

228   proteoliposomes mediated the accumulation of SO_4^{2-} in a time-dependent manner; the uptake

229   occurred rapidly, peaking at about 30 seconds after incubation with the radioligand (Fig. 4d).

230   Consistent with our observations on cells, the influx of sulfate was inhibited by the presence of

231   SO_3^{2-} at micromolar concentrations. *Il*CysZ and *Pf*CysZ exhibited similar uptake profiles in

232   liposomes, suggesting similar functional properties (Fig. 4-S1a).

233

234   To determine whether sulfate uptake by CysZ was driven by the concentration gradient of sulfate

235   itself, or if it was coupled to a secondary driving force such as an ion (e.g., H^+, Na^+) gradient, we

236   tested the effect of the uncouplers CCCP (carbonyl cyanide m-chlorophenyl hydrazone), and

237   oligomycin, as well as that of the ionophores valinomycin and gramicidin on CysZ-mediated

238    $[^{35}S]O_4^{2-}$ accumulation in our cell-based assay (Buckler & Vaughan-Jones, 1998). Since none of

239   these uncoupling agents had a significant effect on the accumulation of $[^{35}S]O_4^{2-}$, these

240   experiments suggest that CysZ-mediated $[^{35}S]O_4^{2-}$ flux is not dependent on the 'classical' H^+ or

241   Na^+ electrochemical transmembrane gradient, thus indicating that the observed uptake solely

242   depends on the SO_4^{2-} transmembrane concentration gradient (Fig. 4-S1b), a notion that is

243   consistent with a channel-like mechanism for CysZ-mediated SO_4^{2-} translocation.

244

245   Finally, we employed the use of single-channel electrophysiological current recordings on CysZ

246   (*Pd*CysZ and *Il*CysZ) reconstituted in a planar lipid bilayer (Fig. 4-S2). Consistent with our

247    $[^{35}S]O_4^{2-}$-based flux assays, these electrophysiological measurements showed that reconstituted

248   CysZ exhibits channel-like properties when a membrane potential is applied in symmetrical

249   Na_2SO_4 solutions on both sides of the bilayer. The *Il*CysZ protein exhibits an average open

250   probability (P_{OPEN}) of 0.8 and conductance estimated as 92 ± 12 pS. However, unitary

251   conductance levels varied, showing a dependence on the amount of protein reconstituted in the

252   planar lipid bilayer. The *Pd*CysZ protein passes a broad distribution of currents at fixed voltages.

11

253   For both proteins, the SO_4^{2-} currents are completely abolished by the presence of low micromolar

254   SO_3^{2-} concentrations.

255

Sulfate Binding Site

257   A bound SO_4^{2-} ion was observed in the structure of *Il*CysZ. This binding site was confirmed by

258   purifying and crystallizing CysZ in the presence of the heavier SO_4^{2-}-analog selenate (SeO_4^{2-}). In

259   the SO_4^{2-} bound structure, each protomer in the dimer showed electron density consistent with a

260   bound sulfate, but only one of the two refined to full occupancy, hence only one is shown in the

261   refined model of *Il*CysZ (Fig. 5a). The location of the bound SO_4^{2-} is close to the putative

262   membrane interface where it is coordinated by two arginine residues (R27 and R28 in *Il*CysZ)

263   and the backbone amides of residues G25 and L26. This SO_4^{2-}-binding site is in the loop between

264   H1 and H2, with the motif GLR(R) being well conserved among the CysZ family. Consistent

265   with this observation, crystals of *Il*CysZ in which R27 and R28 were replaced with alanines did

266   not show interaction with SO_4^{2-} in that site based on i) the lack of any density in the refined

267   mutant structure at 2.3 Å and ii) functional studies (see below). We could not confirm the

268   presence of SO_4^{2-} in either of the other structures of *Pf*CysZ and *Pd*CysZ, owing, at least in part,

269   to their lower resolution limit (~3.5 Å). Soaking and co-crystallization attempts on both *Pf*CysZ

270   and *Pd*CysZ with SeO_4^{2-} resulted in cracking and destabilization of crystals, and loss of

271   measurable diffraction. In this vein, *Il*CysZ R27A/R28A, and the corresponding *Pf*CysZ R25A

272   and *Pd*CysZ R23A mutants all have severely impaired sulfate uptake capability, as demonstrated

273   in cells and proteoliposomes (Fig. 5b, 4-S1a), consistent with a conserved role for these targeted

274   arginine residues in all CysZ variants.

275

12

Conserved core in the hydrophilic head

Each apex of the triangular faces of the *Pd*CysZ hexamer comprises an extra-membranous hydrophilic head of a CysZ protomer (Fig. 1a and 5c). The central core of this hydrophilic head consists of the ends of H3 and H5 and the start of H4, with their residues forming an intricate network of hydrogen bonds and salt bridges that hold this helical bundle together (Fig. 5c). Two highly conserved motifs in this region, ExVE and QYxDYPxDNHK (Fig. 2c), likely play critical roles in this network of interactions. The two aspartates E103 and E106 (*Pd*CysZ) in the first motif interact with R129, N184 and R110, H185, respectively (Fig. 5c). The conserved R129 and R133 on H4b in turn also interact with D183 and N184 in the DNHK sequence stretch of H5b in the second motif. In the second motif, a conserved tyrosine (Y177) lies below the membrane interface towards the core of the molecule, along H5.

Mutational studies on a subset of these conserved hydrophilic-head residues highlight their functional relevance (Fig. 5d). R129 mutants (R129E or Q) exhibited a severe loss of SO_4^{2-} binding and uptake, and mutations made to Q176 and Y177 also showed loss in function, albeit to a lesser extent. Charge reversal mutations made to E103 and E106 (to K or R) or the equivalent *Il*CysZ E107, E110 resulted in very poor expression and stability levels, suggesting that the disruption of the interaction network in this region may destroy the structural integrity of the protein.

Putative pore and sulfate translocation pathway of CysZ

It was already evident from the initial *Il*CysZ structure that the hydrophilic head presented an incipient opening into the membrane, as seen in the center of the Fig. 5c inset, but it was quite

299   unclear how this opening might relate to transmembrane sulfate translocation. The 'transverse'

300   dimer structure of *Pf*CysZ clarified the possibility for ion permeation by showing that openings

301   in its two protomers aligned across the putative membrane; however, the prospective

302   transduction pathway would then be open on one side to the bilayer. The *Pd*CysZ structure

303   showed that the open sides of transverse dimers line a central cavity in the *Pd*CysZ hexamers.

304   Thus, plausible transduction pathways became more evident.

305

306   The view into a protomer surface along the direct pathway between transverse dimer apices (e.g.

307   green to orange in Fig. 3e) displays the pattern of exceptionally high conservation associated

308   with the entrance to a putative pore for sulfate translocation (Fig. 6a, b). This putative entrance

309   or 'pore' lies in the midst of a tight network of interacting residues, which is seen detailed in the

310   inset of Fig. 5c in the very same view as for Fig. 6a. These interactions close the incipient pore

311   from ion conduction in this conformation. The electrostatic potential surface of PdCysZ (Fig. 6c)

312   shows striking and puzzling electronegativity at the conserved pore entrance (Fig. 6d compared

313   with Fig. 6b). Because of the conservations, similar electrostatics pertain to the two other

314   homologs. Moreover, we observe the same helix dispositions, pore shape and charge interactions

315   in all three structures, evident when the protomers are superimposed (Fig. 3c, top view).

316

317   Pathway prediction algorithms (namely, PoreWalker (Pellegrini-Calace, Maiwald, & Thornton,

318   2009)) performed on the CysZ protomer revealed a putative ion translocation pathway that

319   begins at the entrance to the putative pore and ends in the large central cavity of the CysZ

320   hexamer that lies within the membrane (Fig. 7a, b). In the structure of *Pd*CysZ, the entrance of

321   the putative pore appears to be closed by the network of charge-interactions by conserved

322   residues, R110, E106, N184, H185 and W235 (Fig. 6a, 7c-1). These residues interact to tightly

323   restrict access to the putative translocation pathway and constrict the entry of ions, likely

324   selected for size and charge (Fig. 7-S1a). After the narrow entrance, the putative pathway

325   broadens, surrounded by a ring of conserved asparagine and glutamine residues, N33, N91, N98,

326   Q176, and N220 (Fig. 7c-2). Mutations to N98 (N98A, N98D) led to impaired sulfate uptake

327   (Fig. 5d). Following this polar environment, the putative pathway widens even further leading

328   into a large, primarily hydrophobic, internal cavity encapsulated by the TM helices of the

329   PdCysZ hexamer, located in the plane of the lipid bilayer (Fig. 7b, 7-S1c, d). The hydrophobic

330   cavity is enclosed on both the top and bottom by pairs of helices H4-H5, three on each side from

331   the six protomers, pointing in towards the three-fold axis, with each side of the cavity, at its mid-

332   section, measuring ~50 Å, when viewed from above or outside the membrane (Fig. 7-S1c, d).

333   Given the symmetric, dual topology nature of the CysZ assembly, the ions could then exit the

334   cavity via the same pathway as they entered, but traveling through CysZ protomers located on

335   the opposite side of the membrane.

336

337   **DISCUSSION**

338   There are four known families of dedicated SO_4^{2-} transport systems in prokaryotes[6], of which

339   CysZs are the least studied (Zhang et al., 2014). The sequence of CysZ, coding for an integral

340   membrane protein with four predicted TM segments, shows no resemblance to any other known

341   protein. This, and the quest to set the basis for a mechanistic understanding of function,

342   prompted us to investigate the structure of CysZ.

343

344   We present here three structures of CysZ from different species, all determined by x-ray

345   crystallography. These structures are all similar, showing a novel fold comprising two extended

346   TM helices and two hemi-penetrating helical hairpins, giving rise to a tripod-like shape within

347   the membrane, and a hydrophilic head (Fig. 2a, b, 3c). Two of the structures (*Il*CysZ and

348   *Pf*CysZ) show dimers in the crystals, albeit with different interfaces (Fig. 3a, b), and the third

349   structure (*Pd*CysZ) displays a hexameric assembly in multiple crystal forms (Fig. 1a).

350

351   All three structures have a dimeric component, each of which is present in the hexameric

352   arrangement present in all the crystal forms of *Pd*CysZ (Fig. 3a, b), showing how they are all

353   related. Furthermore, *Il*CysZ can be crosslinked in membranes to the alternative *Pf*CysZ dimer

354   by engineering of disulfide cysteine mutants (Fig. 3-S2), which suggests that *Il*CysZ can adopt

355   both of the dimer assemblies observed in the *Pd*CysZ hexamer. Thus, we hypothesize that CysZ

356   is a hexamer in nature, as observed in *Pd*CysZ, and that in the case of *Il*CysZ and *Pf*CysZ, this

357   assembly may have come apart into the subsequently crystallized dimeric components during the

358   process of detergent extraction from the membrane and purification. This could be explained by

359   the unusually labile, and conformationally-flexible, nature of the H4b-H5a helical hairpin of

360   CysZ, with only one pair of stabilizing TM helices per protomer (H2-H3). We presume that the

361   hexamer is maintained with the support and scaffolding of the lipid bilayer.

362

363   CysZ shows a clear dual topology arrangement, which we confirmed with cross-linking

364   experiments on membranes (Fig. 3-S2). Dual-topology insertion is fairly uncommon in

365   membrane proteins; however, reported cases include the well-documented EmrE, a multi-drug

366   resistant export protein that inserts into the membrane as an anti-parallel dimer, and the more

367   recently discovered and studied family of double-barreled 'Fluc' fluoride channels (Amadi,

368   Koteiche, Mishra, & McHaourab, 2010; Korkhov & Tate, 2009; Rapp, Granseth, Seppala, & von

369   Heijne, 2006; Stockbridge et al., 2015; Stockbridge, Robertson, Kolmakova-Partensky, & Miller,

370   2013).

371

372   Functional characterizations of the three CysZs for which we have obtained structural

373   information show that all three mediate SO_4^{2-} uptake and that this uptake is inhibited by SO_3^{2-},

374   for which the protein has higher affinity. Comparable results were obtained in cell-based as well

375   as in proteoliposome-based uptake assays (Fig. 4b, d, 4-S1a). Affinities for SO_4^{2-} and SO_3^{2-} were

376   measured by SPA (Fig. 4c). These results are consistent with previously reported data on *E. coli*

377   CysZ (Zhang et al., 2014). Experiments performed on cells with uncoupling agents (Fig. 4-S1b)

378   showed that CysZ-mediated SO_4^{2-} uptake was independent of a classical electrochemical

379   gradient, thus suggestive of the driving force being a concentration gradient of SO_4^{2-} across the

380   membrane. This hypothesis is supported by our single-channel bilayer experiments performed

381   with *Pd*CysZ and *Il*CysZ, which show that CysZ has channel-like properties (Fig. 4-S2).

382

383   Building on our functional and structural discoveries, our results suggest a fascinating hypothesis

384   for mechanisms of SO_4^{2-} transfer and regulation. There is a conserved central core (Fig. 6a),

385   which is likely to have a structural role. Close to this lies a sulfate-binding site, with functional

386   implications (Fig. 5a), and the entrance to a putative pore (Fig. 5c). The entrance of this putative

387   pore is delineated by a hydrophilic network of conserved residues that form a tight constriction

388   in our observed conformation. Following this hypothetical route, sulfate ions that might enter

389   through the three separate pores, one per CysZ dimer pair, would converge into a central

390   hydrophobic cavity (Fig. 7b, 7-S1c, d). Once sulfate ions enter this central cavity, due to the

391 unfavorable environment, these are likely to exit it rather rapidly through one of the three

392 available exit pores on the cytoplasmic side of the hexamer. Hydrophobic cavities and pores are

393 seen commonly in ion channels, with examples ranging from the well documented hydrophobic

394 inner pores of the various potassium channels (Doyle et al., 1998) to the SLAC1 (Chen et al.,

395 2010) and bestrophin anion channels (Yang et al., 2014), and the MscS and MscL

396 mechanosensitive channels (Anishkin, Akitake, Kamaraju, Chiang, & Sukharev, 2010; Bass,

397 Strop, Barclay, & Rees, 2002; Birkner, Poolman, & Kocer, 2012; Chen et al., 2010; Doyle et al.,

398 1998), facilitating the rapid passage of ions due to the unfavorable environment, as well as

399 potentially providing a means of 'hydrophobic gating' (Aryal, Sansom, & Tucker, 2015).

400

401 The surface electrostatics of CysZ (Fig. 1b and Fig. 6c, d) draw attention to the negative

402 potential of the conserved core of each protomer, which is then surrounded by a more neutral

403 annulus. While this feature seems contradictory to admission of SO_4^{2-} ions at the extracellular

404 side, it could be advantageous for expulsion into the cytoplasm on the opposite side. In any case,

405 the structures that we have determined are evidently in a closed state, implying that a

406 conformational change would have to occur to allow passage of SO_4^{2-}, likely modifying the

407 surface electrostatics of the protein. It is tempting to speculate that the regulation of the opening

408 of the pore could be modulated by the binding of sulfate ions to the identified sulfate-binding

409 site, as it is near the entrance of the putative pore. L22 lies in proximity of the entrance of the

410 putative pore, and its backbone amide (along with G21) coordinates the sulfate ion in the GLR

411 motif of the sulfate-binding site. Thus, the binding of sulfate to the GLR motif could trigger a

412 conformational change needed to displace L22, allowing for a wider opening for the sulfate ions

18

413 to enter the pore. Sulfite could hypothetically exert its inhibitory effect on CysZ function by

414 binding to this site.

415

416 There is an overall electropositive region in the center of the hexameric molecule, when viewed

417 from the top (Fig. 1b, 6c, d). This central region is lined by conserved residues along helices

418 H4b-H5a, namely, R129, R133 and K137. The hydrophobic tips of helices H4b-H5a of the three

419 protomers on each side of the membrane then converge in the center of the hexamer. A pore

420 through the three-fold axis of the hexamer could provide an alternative passageway for SO_4^{2-}

421 ions through this assembly. Although we cannot exclude it, this possibility seems less plausible

422 because of the poor conservation at the tips of helices H4b-H5a and the strictly hydrophobic

423 nature of this region.

424

425 We observe, in agreement with previous data, that SO_3^{2-} inhibits CysZ-mediated SO_4^{2-} flux (Fig.

426 4b, d, 4-S2a, f) (Zhang et al., 2014). The dual topology nature of CysZ could provide a means for

427 internal as well as external regulation. However, experiments in solutions – such as

428 crystallizations – where all molecules are exposed to the same chemical environment, makes

429 capturing such a state in an open or SO_3^{2-} blocked conformation challenging. Despite this

430 limitation, our CysZ structures and associated functional experiments have allowed us to make

431 substantial progress in the understanding SO_4^{2-} uptake by these membrane permeases. This work

432 sets the framework for future experiments aimed at unraveling the molecular details of how

433 SO_4^{2-} is translocated across the membrane by CysZ and how this process is regulated.

434

435 **PDB Accession codes**: *Idiomarina loiheinsis* CysZ: **3TX3**, *Pseudomonas fragi* CysZ: **TBD,**

436 *Pseudomonas denitrificans* CysZ: **TBD**.

437

438 **Materials and Methods**

439

440 **Ortholog selection and cloning**

441 A total of 63 *cysZ* candidate genes were selected by a bioinformatics approach implemented by

442 the New York Consortium of Membrane Protein Structure (NYCOMPS), as previously described

443 (Punta et al., 2009). The majority of the genes (including *Il*CysZ, uniprot ID: Q5QUJ8) were

444 PCR-amplified from fully sequenced prokaryotic genomic DNA (obtained from ATCC®) (Love

445 et al., 2010). CysZ genes from certain species, such as *Pf*CysZ (uniprot ID: A0A0X8F058) and

446 *Pd*CysZ (uniprot ID: M4XKU7) were chemically synthesized by GenScript®, with codon-

447 optimization for protein expression. All genes were cloned by ligation-independent cloning

448 (LIC) (Aslanidis & de Jong, 1990) into an IPTG (isopropyl β-D-1-thiogalactopyranoside)

449 inducible, kanamycin-resistant pET derived plasmid (Novagen), with an N-terminal deca-

450 histidine tag (His10) and a TEV (tobacco etch virus) protease site to allow for tag cleavage upon

451 purification.

452

453 **Protein expression and purification**

454 Expression plasmids bearing the *cysZ* genes were transformed into BL21(DE3)pLysS cells using

455 standard protocols, and grown at 37 °C in 2XYT media supplemented with 50 μg/ml kanamycin

456 and 50 μg/ml chloramphenicol in an orbital shaker at 250 rpm. Protein expression was induced

457 for ~16 hours at 22 °C with 0.2 mM IPTG once an absorbance ($A_{600\ nm}$) of 0.8-1.0 was reached.

20

458   Selenomethione (Se-Met)-incorporated proteins were expressed in BL21(DE3)pLysS cells

459   grown using an M9 minimal media kit (Shanghai Medicilon Inc.) supplemented with the

460   necessary minerals, vitamins and non-inhibitory amino acids. Se-Met was added prior to IPTG

461   induction at an $A_{600\ nm}$ of 1.2. The Se-Met-incorporated protein was purified using the same

462   procedures as the native protein. Once harvested, the cells were resuspended at 0.2 g/ml in lysis

463   buffer containing 20 mM Na-Hepes pH 7.5, 200 mM NaCl, 20 mM MgSO4, DNase I and RNase

464   A, 0.5 mM PMSF (phenylmethylsulfonyl fluoride), EDTA-free Complete protease inhibitor

465   cocktail (Roche) and 1 mM TCEP-HCl (Tris (2-carboxyethyl) phosphine hydrochloride) as a

466   reducing agent. Initial small-scale expression and detergent screening was performed on 80 mg

467   of pelleted cells (wet weight), and 7-10 g of cells for large-scale protein purification. Cells were

468   lysed using an Avestin® EmusiFlex-C3 homogenizer, followed by protein solubilization with 1%

469   (w/v) decyl maltopyranoside (DM) (Anatrace® Affymetrix) for 1 hour at 4 °C, after-which

470   insoluble material was removed by ultra-centrifugation at 100,000 x g. The solubilized protein

471   was applied to Ni-NTA Sepharose (Qiagen) in batch, washed with lysis buffer containing 0.2%

472   DM and 40 mM imidazole and eluted in buffer containing 250 mM imidazole. Upon elution,

473   CysZ was dialyzed overnight with His-tagged TEV protease at 4°C, against a buffer containing

474   20 mM Na-Hepes pH 7.0, 200 mM NaCl, 0.2% DM, 1 mM TCEP-HCl and 20 mM Na2SO4,

475   allowing for the cleavage of the His10 tag and removal of the imidazole. Tagless CysZ was then

476   re-passaged over Ni-NTA sepharose to re-bind of any uncleaved CysZ, TEV protease and the

477   cleaved His10 tag. The protein was then subjected to size-exclusion chromatography (Superdex

478   200 10/30 HR, GE Healthcare) in 20 mM Na-Hepes pH 7.0, 200 mM NaCl, 1 mM TCEP-HCl,

479   20 mM Na2SO4 and appropriate detergent for crystallization, for *Il*CysZ: 0.06% Lauryl

480   dimethylamine oxide (LDAO) and for *Pf*CysZ and *Pd*CysZ: 1% β-octyl glucopyranoside (β-

481   OG). The choice of detergent was made based on protein yield, stability and mono-disperse gel-

482   filtration peaks obtained in the initial small-scale detergent screening. A yield of ~1.5 mg of

483   purified CysZ was typically obtained from a cell pellet of 7-8 grams (1 liter of culture).

484

485   **Protein Crystallization**

486   *Il*CysZ: Crystals of *Il*CysZ in LDAO were obtained by vapor diffusion at a protein concentration

487   of 6-8 mg/ml at 4°C, in a 1:1 v/v ratio against a precipitant of 28-32% PEG400, 0.1M Tris-HCl

488   pH 8.0, with salt additive of 0.1 M NaCl or 0.1 M MgCl$_2$. The crystals appeared overnight,

489   continued to grow in size over the course of 2-4 days after set-up. After optimization, the crystals

490   grew to a maximum size of ~200 μm x 100 μm x 50 μm with a rhomboid or cuboid shape. The

491   crystals were harvested directly without the addition of a cryo-protectant and flash-frozen into

492   liquid nitrogen, for data collection on the X4A/X4C beamlines at National Synchrotron Light

493   Source (NSLS), Brookhaven National Labs (Upton, NY). SeMet derivatized and selenate co-

494   crystals were obtained from the same conditions as the native crystals.

495   *Pf*CysZ: Crystals of *Pf*CysZ in β-OG at 5 mg/ml were initially obtained at 4 °C by vapor

496   diffusion, in a 1:1 protein to precipitant ratio, after 1-2 days against 28% PEG400, 0.1 M MES

497   pH 6.0. They were cuboid in shape and grew in clusters of multiple crystals originating from a

498   common locus. The crystals were optimized to a maximal size of ~150-200 μm x 50 μm x 50

499   μm, with the best diffracting crystals grown under silicone oil (visc. 500) in microbatch Terazaki

500   plates. Crystals were directly flash-frozen into liquid nitrogen without the use of a cryo-

501   protectant and were exposed to X-rays at the NE-CAT (241DC and E) beamlines at APS,

502   Argonne National Lab (Argonne, IL) for data collection. SeMet crystals were obtained from the

503   same conditions as the native protein.

504 *Pd*CysZ: Crystals of *Pd*CysZ in β-OG at 5-8 mg/ml were initially obtained at 4°C by vapor

505 diffusion, in a 1:1 protein to precipitant ratio, after 2-3 days against 22-30% PEG550MME, 0.1

506 M Na-Hepes pH 7.0. The rod-like crystals were hexagonal on one face, and grew in clusters

507 originating from a common locus as well as on the edge of the drop. The multiple crystal forms

508 observed were all obtained in the same crystallization conditions. The crystals were optimized to

509 a maximal size of ~200-250 μm x 25 μm x 50 μm. With the addition of 20% glycerol (w/v) as a

510 cryo-protectant, the crystals were flash-frozen into liquid nitrogen and were exposed to X-rays at

511 the NE-CAT (24-IDC and 24-IDE) beamlines at APS, Argonne National Lab (Argonne, IL) for

512 data collection.

Data collection and structure determination

514 *Il*CysZ: The structure of CysZ was determined by the single-wavelength anomalous diffraction

515 (SAD) method from anomalous diffraction of a selenate (SeO_4^{2-}) derivative crystal. The

516 anomalous signals were measured at the Se K-edge peak wavelength, which was determined

517 experimentally from fluorescence scanning of the crystal prior to data collection. All diffraction

518 data were recorded at 100K using an ADSC Q4R CCD detector at the NSLS X4 beamline.

519 Diffraction data were indexed, integrated, scaled, and merged by HKL2000 (Otwinowski &

520 Minor, 1997). Selenate substructure determination was performed with the SHELXD program

521 through HKL2MAP (Pape & Schneider, 2004). A resolution cut-off at 2.6 Å was used for

522 finding Se sites by SHELXD. A strong peak found by SHELXD was used to calculate initial

523 SAD phases, which were improved by density modification by SHELXE (Sheldrick, 2010). With

524 a solvent content of 65% corresponding to 2 molecules in the asymmetric unit, 50 cycles of

525 density modification resulted in an electron density map of sufficient quality for model building.

526 The initial polypeptide chain was built by Arp/Warp (Langer, Cohen, Lamzin, & Perrakis, 2008),

527   at 2.1 Å by using experimental phases. Further cycles of model building were performed

528   manually using COOT (Emsley, Lohkamp, Scott, & Cowtan, 2010) and all rounds of

529   refinements were performed with PHENIX (Adams et al., 2010). The native structure of CysZ

530   with bound sulfate was determined both by multi-crystal native SAD (Liu et al., 2012) (final

531   resolution of 2.3 Å) and by molecular replacement with the selenate bound model (final

532   resolution of 2.1 Å). In addition, phase information obtained from Se-Met derivatized protein

533   with 9 Se sites per CysZ molecule, verified our model obtained from the selenate data.

534

535   *Pf*CysZ: Multi-crystal SeMet-SAD data sets were collected at APS beamline 24-IDC with a

536   Pilatus 6M pixel array detector under a cryogenic temperature of 100 K. To enhance anomalous

537   signals from Se atoms for phasing (Liu, Zhang, & Hendrickson, 2011), the X-ray wavelength

538   was tuned to the Se-K edge (λ=0.9789 Å). The orientation of crystals was random without

539   special consideration of crystal alignment, and beam size was adjusted to match the crystal size.

540   A total of 22 data sets were collected, each from a single crystal. An oscillation angle of 1° was

541   used for data collection with a total of 360 frames for each data set. The beam size was adjusted

542   to match the crystal size. The 22 single-crystal data sets were processed individually by using

543   XDS (Kabsch, 2010) and CCP4 packages (Winn et al., 2011). For phasing purposes, the low-

544   resolution anomalous signals were enhanced by increased multiplicity. By rejection of 7 outlier

545   crystals (Liu et al., 2012), anomalous diffraction data from 15 statistically-compatible crystals

546   were scaled and merged for phasing. For outlier rejection, a unit-cell variation of 1.0σ was used.

547   CCP4 program POINTLESS and SCALA (Evans, 2006) were used for data combining; and

548   Bijvoet pairs were kept separately throughout the data flow. For refinement purposes, keeping

549   the high angle data was important, and done by limiting radiation damage as well as by

550 increasing multiplicity. Although most *Pf*CysZ crystals diffracted to only about 3.5 Å spacings

551 or poorer, we intentionally set the detector distance to include higher spacings. Higher resolution

552 data were retained through a data merging procedure that is described as follows: 1) The 22

553 individually processed data sets were analyzed by diffraction dissimilarity analysis by using only

554 high angle data between 3.5-3.0 Å, resulting in three subsets. 2) The data statistics of members in

555 each subset were checked manually and the subset that contained the highest angle data set, e.g.

556 data set 6, was selected for further analyses and data combination. 3) Each data set within the

557 selected subset was compared with data set 6 by high-angle intensity correlation. Six of the

558 highest resolution data sets were statistically comparable and therefore were selected for

559 merging. For phasing, substructure solutions were found by SHELXD (Sheldrick, 2010) and

560 were further refined and completed by PHASER (McCoy et al., 2007) and then used to compute

561 initial SAD phases at the data limit by SAD phasing with PHENIX (Adams et al., 2010). Phases

562 were density modified with solvent flattening and histogram matching as implemented in CCP4

563 program DM (Cowtan & Zhang, 1999) to improve phases and also to break phase ambiguity.

564 The estimated solvent contents of 71% were used for density modification. The model was

565 initially built into the experimental electron density map by COOT (Emsley et al., 2010),

566 followed by iterative refinement by PHENIX and model building in COOT. The refined model

567 does not contain solvent molecules at this resolution.

568

569 *Pd*CysZ:

570 Native crystal data were collected at the APS beamline 24-IDC with a Pilatus 6M pixel array

571 detector at a cryogenic temperature of 100 K at an X-ray wavelength of λ=1.023 Å. The sample-

572 to-detector distance was set to 500 mm. An oscillation angle of 0.5° was used for data collection.

573   The beam size was adjusted to match the crystal size. Molecular replacement was attempted

574   using a variety of search models (*Pf*CysZ and *Il*CysZ monomer/dimer models, with various

575   degrees of truncation). Success was achieved by searching for six copies of a search model

576   consisting of the *Pf*CysZ monomer, with residues 36-53 deleted and the sequence adjusted using

577   CHAINSAW (Stein, 2008) (pruning non-conserved residues to the gamma carbon). Density

578   modification of the initial map was performed in PARROT, incorporating solvent flattening,

579   histogram matching and NCS-averaging. An initial round of model building was performed in

580   COOT (Emsley et al., 2010) into this map, followed by further phase improvement and bias-

581   removal using *phenix.prime_and_switch* (Adams et al., 2010*)*. The improved map was used for a

582   second round of model building, followed by iterative cycles of reciprocal space refinement

583   using *phenix.refine*, and real-space refinement and correction in COOT.

584   All graphical representations and figures of our structural models were made in either PyMOL

585   (Schrodinger, 2010) or Chimera (Pettersen et al., 2004).

586

587   **Radioligand Binding by Scintillation Proximity Assay (SPA)**

588   CysZ was purified by standard protocols as described above, with the exception of leaving the

589   histidine-tag intact without cleavage by the TEV protease. The imidazole was removed by

590   dialysis and the purified protein was not run over the size exclusion column, and instead was

591   directly concentrated to 2 mg/ml for the SPA experiment. $[^{35}S]O_4^{2-}$ obtained in the form of

592   sulfuric acid (American Radiolabeled Chemicals (ARC)) was used as the radioligand. 100 ng –

593   250 ng of CysZ was used per assay point, diluted in 100 μl of assay buffer containing 20 mM

594   Hepes pH 7.0, 200 mM NaCl, 0.2% DeM, 20% glycerol, 0.5 mM TCEP, with 12.5 μl of Copper

595   YSi beads (Perkin Elmer). A trace amount of $[^{35}S]O_4^{2-}$ (~10-30 nM) mixed with cold ligand

596 (Na_2SO_4) was added to each well of a 96 well clear bottom plate along with the mix of protein,

597 buffer and beads. The plate was agitated for a minimum of 30 minutes to as long as overnight,

598 and measured in a scintillation counter the following morning (MicroBeta, Perkin Elmer).

599 Competitive binding experiments with a gradient of a competing cold ligand ranging from (10

600 nM – 100 mM) were performed in triplicate, with the control measured at each concentration by

601 adding 1 M Imidazole to the reaction buffer, to prevent binding of the protein to the scintillation

602 beads. All data were analyzed and graphically represented with GraphPad™ Prism6 software.

603

604 **$[^{35}S]O_4^{2-}$ Uptake Experiments**

605 *In whole cells:* The *cysZ* gene knockout strain in *E. coli* K-12 was obtained from the Coli

606 Genetic Stock Center at Yale University (http://cgsc.biology.yale.edu/), originally found in the

607 Keio knockout collection (Baba et al., 2006). Genotype: F-, Δ(araD-araB)567, Δ

608 lacZ4787(::rrnB-3), λ-, ΔcysZ742::kan,rph-1, Δ(rhaD- rhaB)568, hsdR514. The knockout

609 strain was made competent by standard protocols (Hanahan, 1983) to allow for the

610 transformation and expression of *cysZ*-containing plasmids, for rescue experiments. Wild-type

611 parental *E. coli* K-12 was used as a control strain. The strains were grown in LB (Luria Broth)

612 without any antibiotic (for the WT cells) and with 50 μg/ml of kanamycin for the knockout cells

613 at 37 °C overnight to saturation. The culture was spun down at 3000 x g the next morning and

614 the cells were resuspended in Davis-Mingioli (DM) minimal media without sulfate ($MgSO_4$ was

615 replaced with $MgCl_2$ and $(NH_4)_2SO_4$ was replaced by NH_4Cl), supplemented with 0.63 mM L-

616 cysteine to allow the cells to grow in the absence of sulfate (Davis & Mingioli, 1950). The cells

617 were incubated in DM media for a minimum of 9 hours, maximum overnight, at 37°C after

618 which they were spun down and washed 3 times in 5 mM Na-Hepes pH 7.0. This ensured that

619   the cells were starved of SO_4, to deplete the sulfate stores in the cell, enhancing sulfate uptake

620   measured (F. Parra, personal communication). The cells were resuspended in the same buffer at

621   0.7 g/ml at room temperature, and 10 μl of the cell suspension was used for each point in the

622   uptake experiment. A final concentration of 320 μM of SO_4 (Na_2SO_4 with $[^{35}S]O_4^{2-}$ as a tracer)

623   was used outside. The uptake experiments were performed in triplicate, measured over a time

624   course of typically 0 - 300 seconds. The reaction was stopped by dilution, by adding 1.5 ml of

625   ice-cold buffer (5 mM Na-Hepes pH 7.0) to the cells in the tube. The reaction mix was

626   immediately poured onto a vacuum filtration device, with an individual glass-fiber filter (0.75

627   μm, GF/F) per assay point, after which the filters are washed once more with 1.5 ml of buffer.

628   The dry filters, with the cells attached to their surface, were then moved to scintillation vials,

629   containing 4 ml of EconoSafe® scintillation cocktail, to be counted the next morning. For the

630   *CysZ* cell rescue experiments, a similar protocol was used, transformed with an ampicillin

631   resistant expression vector containing the CysZ gene, mutant or empty vector (as the control).

632   Upon transformation, the cells were grown overnight in a 4 ml starter culture of LB with 50

633   μg/ml kanamycin and 100 μg/ml ampicillin. The next morning the entire 4 ml was used to

634   inoculate 75 ml of LB (Kan, Amp), and grown at 37 °C for 2.5-3 hours until an OD_{600} of 0.6-0.8

635   was reached. Protein expression was then induced at 37 °C for 4 hrs with 0.2 mM IPTG. After

636   4hrs, the cells were spun down and resuspended in the DM minimal media without sulfate, 0.63

637   mM cysteine, Amp, Kan and 0.2 mM IPTG, and incubated overnight at 22 °C. The next morning

638   the cells were spun down, washed 3 times with 5 mM Na-Hepes 7.0 and resuspended at final

639   concentration of 0.7 g/ml for uptake.

640   *In proteoliposomes:* CysZ was purified by the procedure described above, and upon elution from

641   the size-exclusion column concentrated to 1 mg/ml for reconstitution into liposomes at a protein

642   to lipid ratio of 1:100. The liposomes were comprised of a 3:1 ratio of *E. coli* polar lipids and

643   phosphatidylcholine (PC) (Avanti Polar Lipids), prepared by previously described methods

644   (Rigaud, Pitard, & Levy, 1995). Typically, 10 μl of CysZ-proteoliposomes and control 'empty'

645   liposomes at a concentration of 5-10 mg/ml, were used per assay point and diluted into a reaction

646   buffer of 100 μl, containing $[^{35}S]O_4^{2-}$ (at trace amounts of ~10-15 nM) supplemented with

647   Na_2SO_4 at the desired concentration. The experiment was performed in triplicate and sulfate

648   accumulation was measured either over a time-course or at a fixed time with different amounts

649   of SO_4^{2-} or SO_3^{2-} present. The reaction was stopped by dilution, by adding 1.5 ml of ice-cold

650   buffer (5 mM Na-Hepes pH 7.0) to the cells in the tube. The reaction mix was immediately

651   poured onto a vacuum filtration device, with an individual nitrocellulose filter (0.22 μm) per

652   assay point, after which the filters are washed once more with 1.5 ml of buffer. The dry filters,

653   with the cells attached to their surface, were then moved to scintillation vials, containing 4 ml of

654   EconoSafe® scintillation cocktail, to be counted the next morning.

655   **Measurement of CysZ single-channel activity in the planar lipid bilayer**

656   A previously described method (Mueller, Rudin, Tien, & Wescott, 1962) to insert ion channels

657   incorporated in liposomes into "painted" planar lipid bilayers by vesicle fusion was used to

658   incorporate CysZ into a lipid bilayer created on a small aperture between two aqueous

659   compartments, called the cis and trans compartments (Morera, Vargas, Gonzalez, Rosenmann, &

660   Latorre, 2007). Since this system is very sensitive to contaminants, CysZ was expressed in and

661   purified from a porin- deficient strain of *E. coli* cells to prevent any carry through of

662   contaminating porins that could create large conductances and artifacts in the single-channel

663   recordings. Phosphatidylethanolamine (PE) and phosphatidylserine (PS) (Avanti Polar Lipids),

664   in a ratio of 1:1 were dissolved in chloroform to mix, and dried completely under an argon

29

665   stream. The mixed and dried lipids were then dissolved in n-decane to a final concentration of 50

666   μg/ml, and kept at 4 °C. The lipids are always prepared fresh, on the same day of the experiment.

667   The purified CysZ protein were incorporated into PE:PS (1:1) liposomes by brief sonication at

668   80kHz for 1 minute at 4 °C. The experimental apparatus consisted of two 1-ml buffer chambers

669   separated by a Teflon film that contains a single 20- to 50-μm hole. A lipid bilayer was formed

670   by "painting" the hole with the 1:1 mixture of PE:PS, this results in a seal between the two cups

671   formed by the lipids (Leal-Pinto, London, Knorr, & Abramson, 1995). For these studies, the cis

672   side was defined as the chamber connected to the voltage-holding electrode and all voltages are

673   referenced to the trans (ground) chamber. Stability of the bilayer was determined by clamping

674   voltage at various levels. If a resistance $> 100 \ \Omega$ and noise < 0.2 pA were maintained in the

675   patch, the proteoliposomes containing CysZ were added to the trans side of the chamber and

676   stirred for 1 min. The fusion event or insertion of a channel into the bilayer was assessed by the

677   presence of clear transitions from 0 current to an open state.

678

679   **Site-specific cysteine labeling experiments**

680   All functional and cysteine mutants of CysZ were generated by site-directed mutagenesis, using

681   the QuikChange® site-directed mutagenesis kit (Strategene). The sequence-verified mutants

682   were then tested for expression in comparison to the WT CysZ. To address the membrane

683   topology of *Il*CysZ, single cysteine mutants were designed to perform site-directed fluorescence

684   labeling based on the accessibility of the cysteine to the membrane impermeable thiol-directed

685   fluorescent probe (Ye, Jia, Jung, & Maloney, 2001). A set of surface-exposed residues at

686   different positions on the CysZ molecule were selected to be mutated to cysteines, based on the

687   *Il*CysZ structure. The cysteine mutants were expressed by standard protocols that were used for

688   the WT protein. The membrane fraction of each mutant was pelleted after cell lysis by

689   ultracentrifugation at 100,000 x g and resuspended at 20 mg/ml (Bradford assay) in fresh buffer

690   containing 20 mM Na-Hepes pH 7.0, 200 mM NaCl, protease inhibitors: 0.5 mM PMSF and

691   Complete protease inhibitor cocktail EDTA-free and 1 mM TCEP-HCl. 1 ml of membranes were

692   then incubated with 30 μM membrane-impermeant fluorescein-5-maleimide dye (Invitrogen, 2

693   mM stock freshly prepared in water, protected from light) for 30 minutes in the dark at room

694   temperature. The labeling reaction was stopped by the addition of 6 mM β- mercaptoethanol, and

695   the membranes were spun down and resuspended in fresh buffer to remove any remaining

696   unreacted fluorescent dye. The fluorescently labeled protein was then purified from the

697   membranes by solubilization with 1% DM, using a standard Ni-NTA purification protocol,

698   qualitatively analyzed on an SDS-PAGE, and quantitatively measured by a Tecan® fluorescence

699   plate reader at an excitation of 495 nm, emission of 535 nm.

700

701   **Crosslinking of Cysteine Mutant Pairs in CysZ**

702   Cysteine mutants of *Pf*CysZ and *Il*CysZ were designed based on pairs of residues that were in

703   close proximity (within 3-7 Å) of each other in our structure that could have the ability to

704   covalently join the 2 protomers of the dimer. The single and double cysteine mutants were made

705   by site-directed mutagenesis using the QuikChange® Site-Directed Mutagenesis Kit

706   (Strategene). Mutants and WT were expressed using the standard protocols CysZ expression.

707   Isolated membrane fraction was resuspended by homogenization in fresh lysis buffer at a

708   membrane protein concentration of ~25 mg/ml (measured by Bradford Assay). Bis-

709   methanethiosulfonate (Bis-MTS) crosslinkers (Santa Cruz Biotechnolgies) of different spacer

710   lengths were used at 0.5mM (dissolved in DMSO) added to 1ml of resuspended membranes at

31

711 RT for 1 hour. Bis-MTS crosslinkers are membrane permeable, highly reactive and specific to

712 sulfhydryl groups, and the covalent linkage is resistant to reducing agents like β-mercaptoethanol

713 (Akabas, Stauffer, Xu, & Karlin, 1992). The crosslinking lengths used were: 1,1-Methanediyl

714 Bismethanethiosulfonate (3.6 Å), 1,2- Ethanediyl Bismethanethiosulfonate (5.2 Å), 1,4-

715 Butanediyl Bismethanethiosulfonate (7.8 Å) and 1,6-Hexanediyl Bismethanethiosulfonate (10.4

716 Å). The reaction was quenched by the addition of 10 mM free cysteine, and the protein was then

717 extracted and purified from the membranes with 1% DM followed by Ni-NTA resin. The

718 imidazole is then diluted out in the Ni-elute, and the His-tag is cut with TEV protease in small

719 scale. The cleaved protein is passaged over Ni-NTA resin to remove contaminants and uncleaved

720 protein, and flowthrough is run on a reducing SDS- PAGE and stained with Coomassie blue to

721 analyze dimer formation. The mutants designed were L161C (single mutant), L161C-A164C and

722 N160C-L168C (double mutants) for *Pf*CysZ; and L156C-Q163C and V157C-Q163C (double

723 mutants) for *Il*CysZ.

724

725 **Acknowledgments:**

32

738

739   Declaration of Competing Interests:

740   The authors declare that they have no financial or non-financial competing interests.

741   **Figures and Tables:**

742   **Table 1: Crystallographic data and refinement statistics.**

743

Data collection	Native *IlCysZ*	*IlCysZ* w/SeO$_4^{2-}$ (SAD)	SeMet *PfCysZ* (6 crystals, refinement)	SeMet *PfCysZ* (15 crystals, SAD)	Native *PdCysZ* (MR-SAD)
Beamline	NSLS X4A	NSLS X4A/C	APS 24-ID-E	APS 24-ID-C	APS 24-ID-C
Space group	C2	C2	C2	C2	P6$_3$
Cell dimensions:					
a, b, c (Å)	128.9, 82.0, 100.4	128.9, 81.9, 100.3	172.29, 56.9, 96.17	172.35, 56.9, 96.31	225.13, 225.13, 96.62
α, β, γ (°)	90, 125.1, 90	90, 125.1, 90	90, 91.43, 90	90, 91.33, 90	90, 90, 120
Z$_a$	2	2	2	2	6
Wavelength	1.7432	0.96789	0.97890	0.97890	1.0230
Bragg spacings (Å)	30-2.30	50-2.10	40-3.20	40-3.50	86-3.40
R$_{merge}$	0.047 (0.257)	0.046 (0.417)	0.136 (6.506)	0.135 (2.13)	0.095 (2.89)
I / σ$_I$	29.4 (7.9)	25.0 (1.9)	12.3 (0.7)	24.2 (2.6)	22.4 (1.2)
Completeness (%)	99.9 (99.9)	99.9 (100.0)	99.8 (99.3)	99.9 (100.0)	100.0 (100.0)
Multiplicity	7.3 (7.2)	7.6 (7.6)	27.2	72.8	19.7
Refinement:					
Resolution (Å)	2.30		3.50		3.40
No. of reflections	38075		20741		37221
R$_{work}$ / R$_{free}$	0.200/0.238		0.297/0.339		0.239/0.277
No. of atoms:					
Protein	3679		3428		11415
Ligand/ion	249		0		560
Water	162		0		0
Average B-factors (Å^2)	49.4		198.9		204.18
Protein	48.4		198.9		204.18
Ligand/Ion	77.3		-		-
Water	45.3		-		-
Bond Ideality (r.m.s.d.):					
Bond lengths (Å)	0.006		0.006		0.004
Bond angles (°)	0.894		1.133		0.96
Ramachandran Analysis:					
Favored (%)	99.0		99.2		98.5
PDB accession code	3TX3		TBD		TBD

744
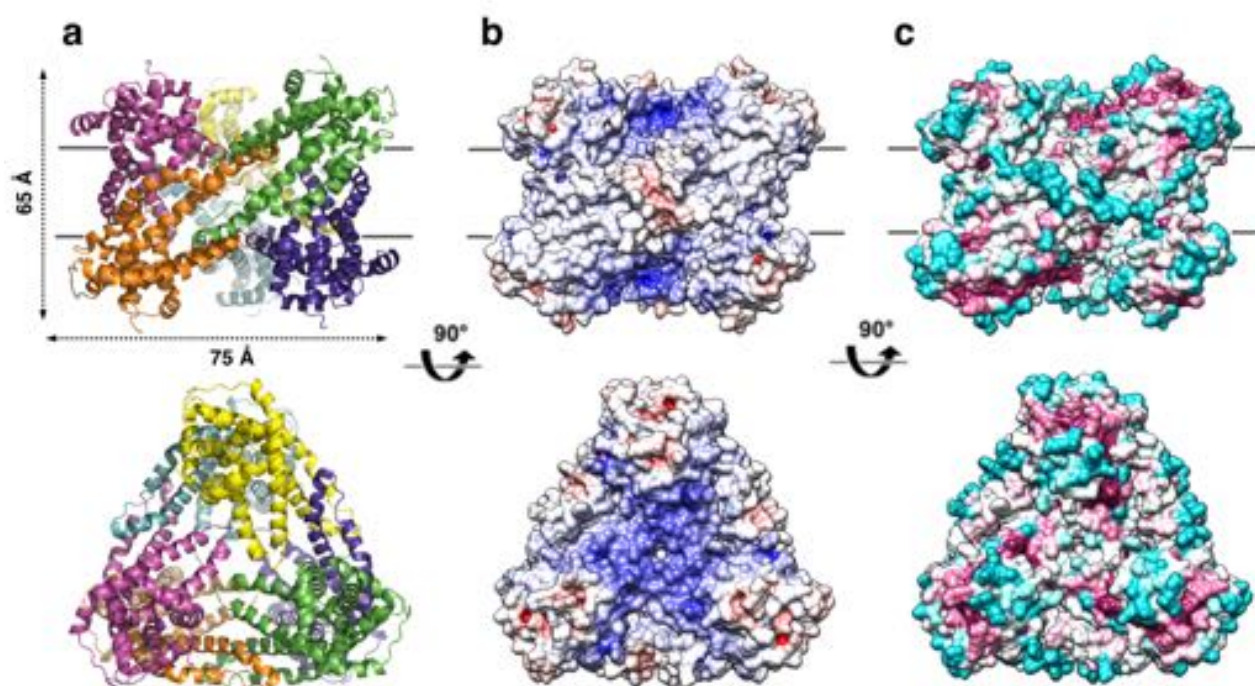
745   Values in parentheses are from the highest resolution shell. R$_{free}$ was calculated using 5% of data

746   excluded from refinement.

747

748

34

749 **Figure 1.**

750

751

752 **Fig. 1. Overall structure of the *P. denitrificans* CysZ (*Pd*CysZ) hexamer.** a. Side and top

753 views of the hexamer as a ribbon diagram with each protomer chain colored differently. The

754 approximate dimensions of the hexamer marked in Å. b. Side and top views represented by

755 surface electrostatics as calculated by APBS, with negative and positive surface potential

756 represented in red and blue respectively. c. Side and top views representing conservation of

757 residues as calculated by ConSurf, with maroon being most conserved to cyan being least

758 conserved.

759

760 **Figure 1 – Figure Supplement 1.**
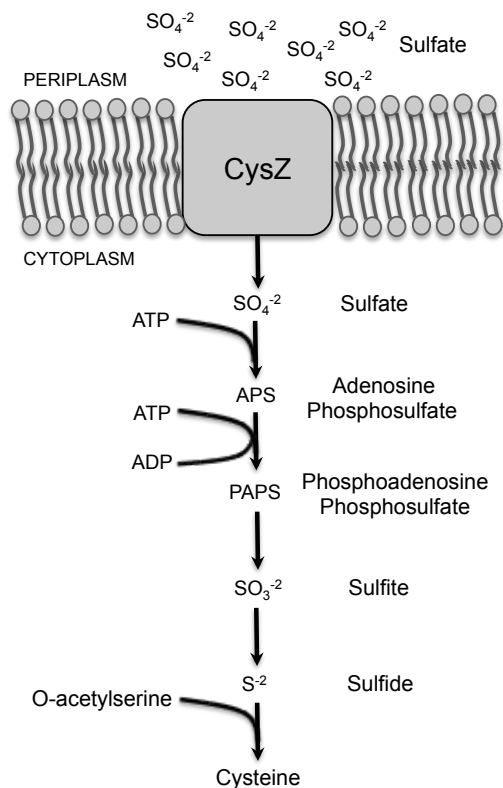
761

762

763 **Fig. 1. S1. Schematic of assimilatory sulfate reduction in bacteria for cysteine biosynthesis.**

764 Assimilatory reduction is energetically dispendious as sulfate is extremely stable. In this

765 pathway, sulfate ions enter the cell via a transporter or channel, like CysZ; this is followed by its

766 activation by ATP-sulfurylase, which utilizes ATP to form adensosine phosphosulfate (APS) and

767 inorganic pyrophosphate (PPi) as a by-product. APS is then further activated by the addition of a

768 second phosphate forming phosphoadenosine phosphosulfate (PAPS) and this high-energy

769 intermediate product is poised for sulfur removal to form sulfite ($SO3^{2-}$) by the thioredoxin

770 enzyme, which is then further reduced to sulfide ions (S^-). Sulfide, the final reduced sulfur

771 product, can then be used in a variety of ways by the cell, such as the incorporation into O-

772 acetylserine to synthesize cysteine.

36

773 **Figure 1 – Figure Supplement 2.**

a

b
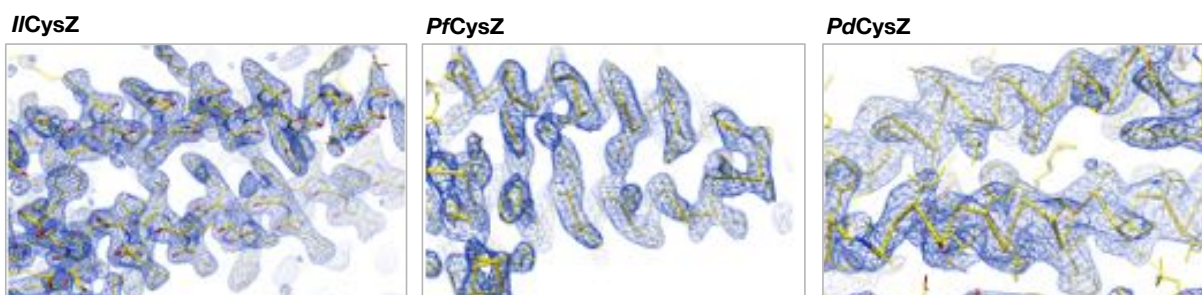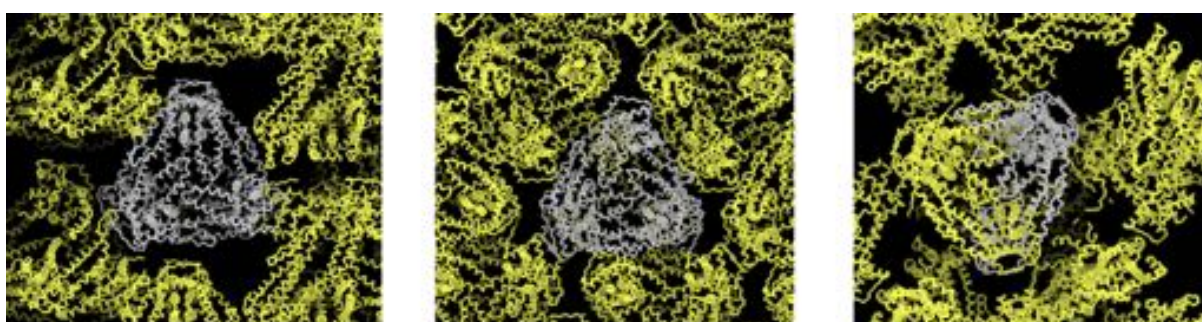
774

775

776 **Fig. 1. S2. Representative electron density of the crystal structures of *Il*CysZ, *Pf*CysZ and**

777 ***Pd*CysZ, and the different crystal forms observed for *Pd*CysZ.** a. Representative electron

778 density in blue mesh for: *Il*CysZ, contoured at 1 x r.m.s.d., *Pf*CysZ, contoured at 2 x r.m.s.d, with

779 a negative B-factor of -100 Å^2 applied to map; *Pd*CysZ, contoured at 1 x r.m.s.d, with a negative

780 B-factor of -100 Å^2 applied to map. Final atomic models (Cα trace with side chains depicted) are

781 shown as yellow stick representation. b. Preliminary molecular replacement analyses of the 3

782 different crystal forms obtained for *Pd*CysZ, showing the hexameric assembly of the molecule,

783 seen in each case. The Cα trace of an asymmetric unit in each case is depicted in grey, with their

784 symmetry mates are shown in yellow. Space group and unit cell dimensions are listed below.

37

785   **Figure 2.**

786

787

788   **Fig. 2. Structure and topology diagram of *Pd*CysZ protomer, with sequence alignment and**

789   **conservation** a. Ribbon diagram of the *Pd*CysZ protomer colored in rainbow colors from N

790   (blue) to C terminus (red), viewed from within the plane of the membrane, shown in the same

791   orientation as the protomer drawn in green in Fig. 1a. b. Topology diagram of the *Pd*CysZ

792   protomer with helices marked from 1 to 8. Helices H2b and H3a are transmembrane helices,

793   whereas H4-H5 and H7-H8 are hemi-penetrating helical hairpins, only partially inserted into the

38

794   membrane. c. Sequence alignment of *E. coli* CysZ (*Ec*CysZ), *P. denitrificans* CysZ (*Pd*CysZ), *P.*

795   *fragi* CysZ (*Pf*CysZ), and *I. loihiensis* CysZ (*Il*CysZ). Residues are colored based on

796   conservation, with maroon being most conserved and cyan least conserved, as calculated by

797   ConSurf using a sequence alignment of 150 non-redundant sequences from the CysZ family as

798   input. Spirals above residues mark the extent of the helical segments based on the atomic

799   structure of *Pd*CysZ with helices numbered H1-H8; letters mark residue identities; black dots

800   above identify every tenth residue (modulo 10) in the *Pd*CysZ sequence and black underlines

801   mark functionally relevant motifs discussed in the text.

802 **Figure 3.**
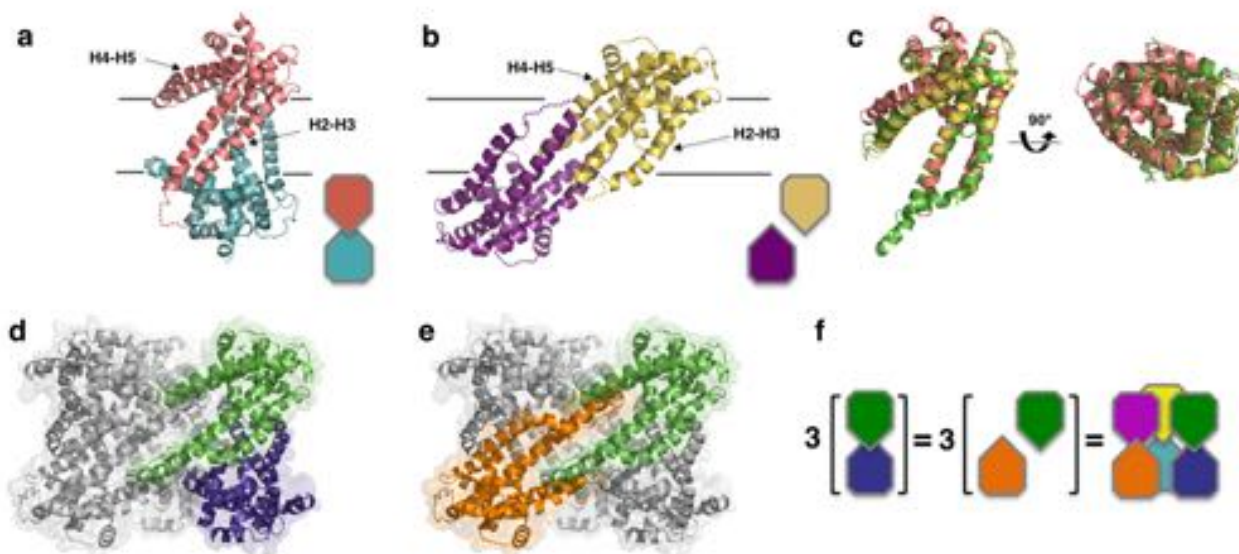
803

804

805 **Fig. 3. Structures of *Il*CysZ and *Pf*CysZ, with comparison to *Pd*CysZ** a. Ribbon diagram of

806 the structure of CysZ from *I. loihiensis (Il*CysZ) at 2.3 Å. Protomers of the dimer are colored in

807 salmon pink and teal blue, arranged in a head-to-tail conformation in the membrane, with helical

808 hairpins H2-3 and H4-5 labeled for clarity. The dimer interface of *Il*CysZ involves H2-3. b.

809 Ribbon diagram of the structure of CysZ from *P. fragi (Pf*CysZ*)* at 3.2 Å. The protomers of the

810 dual topology dimer in the membrane are colored gold and purple, with helical hairpins H2-3 and

811 H4-5 again labeled. The dimer interface here involves the interaction of helices H4-5 of each

812 protomer. c. Side and top views of the superposition of the three different protomers from

813 *Pd*CysZ (green), *Il*CysZ (pink) and *Pf*CysZ (yellow) after aligning H1-H3. d, e. The same dimer

814 interfaces observed in *Il*CysZ (a) and *Pf*CysZ (b) observed in the hexameric assembly of

815 *Pd*CysZ, as highlighted in green and blue (d) and green and orange (e). f. Schematic

816 representation showing how three copies of the dimeric protomers of *Il*CysZ (green and blue,

40

817   left) and of *Pf*CysZ (orange and green, center), can coexist in and each recapitulate the

818   hexameric assembly of *PdCysZ*.

819 **Figure 3 – Figure Supplement 1.**

820

*Pd*CysZ   *Il*CysZ   *Pf*CysZ

821

822
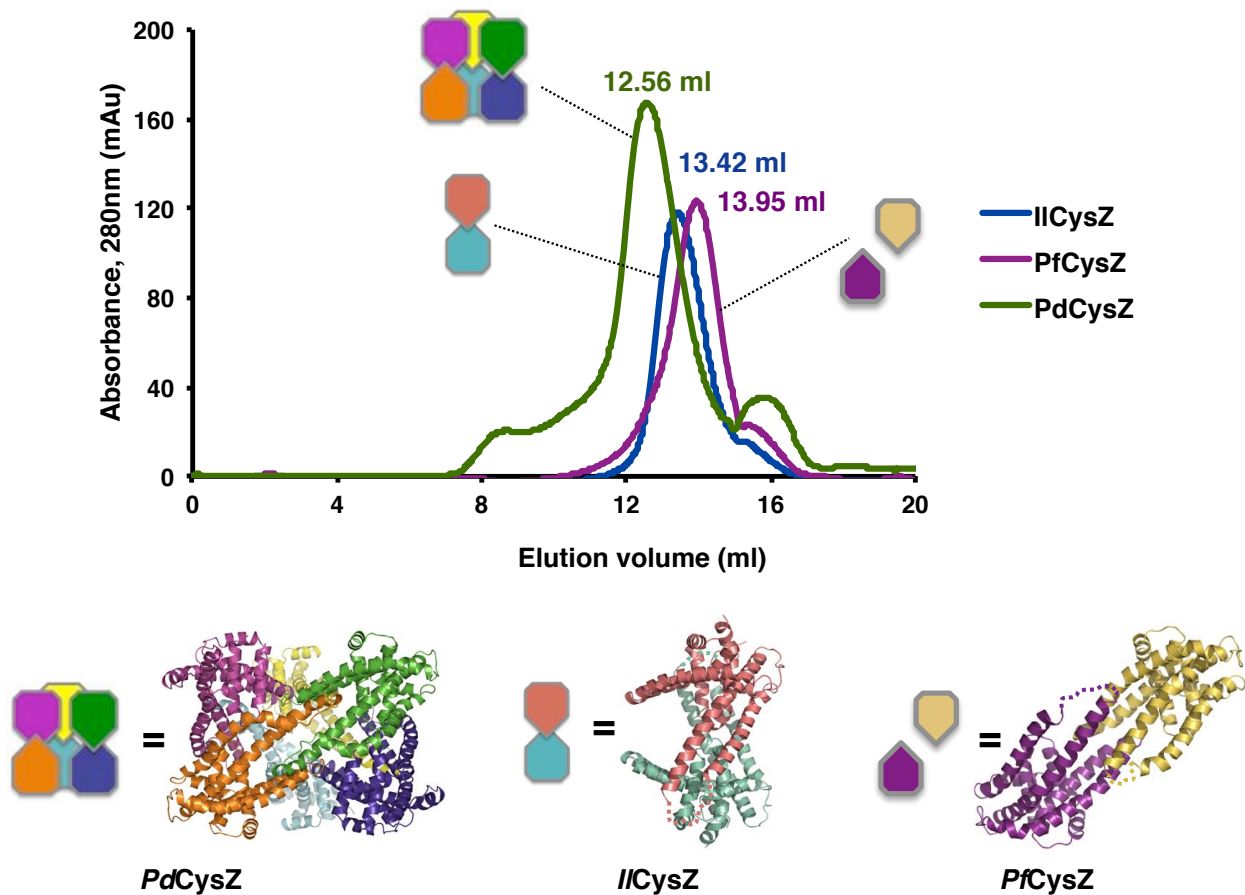
823 **Fig. 3. S1. Size-exclusion chromatography of CysZ shows a mono-disperse elution profile**

824 **for each of the three species purified - *Pd*CysZ, *Pf*CyZ and *Il*CysZ.** All three proteins were

825 solubilized from isolated membrane fractions purified in the presence of 0.2% decyl

826 maltopyranoside (DeM) and exchanged into buffer containing 1% β-octyl glucopyranoside (β-

827 OG) on the size-exclusion column (Superdex 200 10/30 HR). A schematic of the oligomeric

828 states observed in the three crystal structures of CysZ are shown below the elution profiles.

829 Crystallization trials were set-up directly after the size-exclusion chromatography step. A shift of

830   ~1 ml was observed for the elution of *Pd*CysZ (peak at 12.56 ml), with respect to *Pf*CysZ and

831   *Il*CysZ, indicating that the size (volume) and shape of *Pd*CysZ is significantly larger than the

832   other two species. *Il*CysZ elutes at 13.42 ml, 0.5 ml ahead of *Pf*CysZ, which could be explained

833   by the shape of *Il*CysZ, occupying more volume as compared to *Pf*CysZ, with its helices (H4-

834   H5) pointing outward, away from the body of the dimer.

835

43

836 **Figure 3 – Figure Supplement 2.**
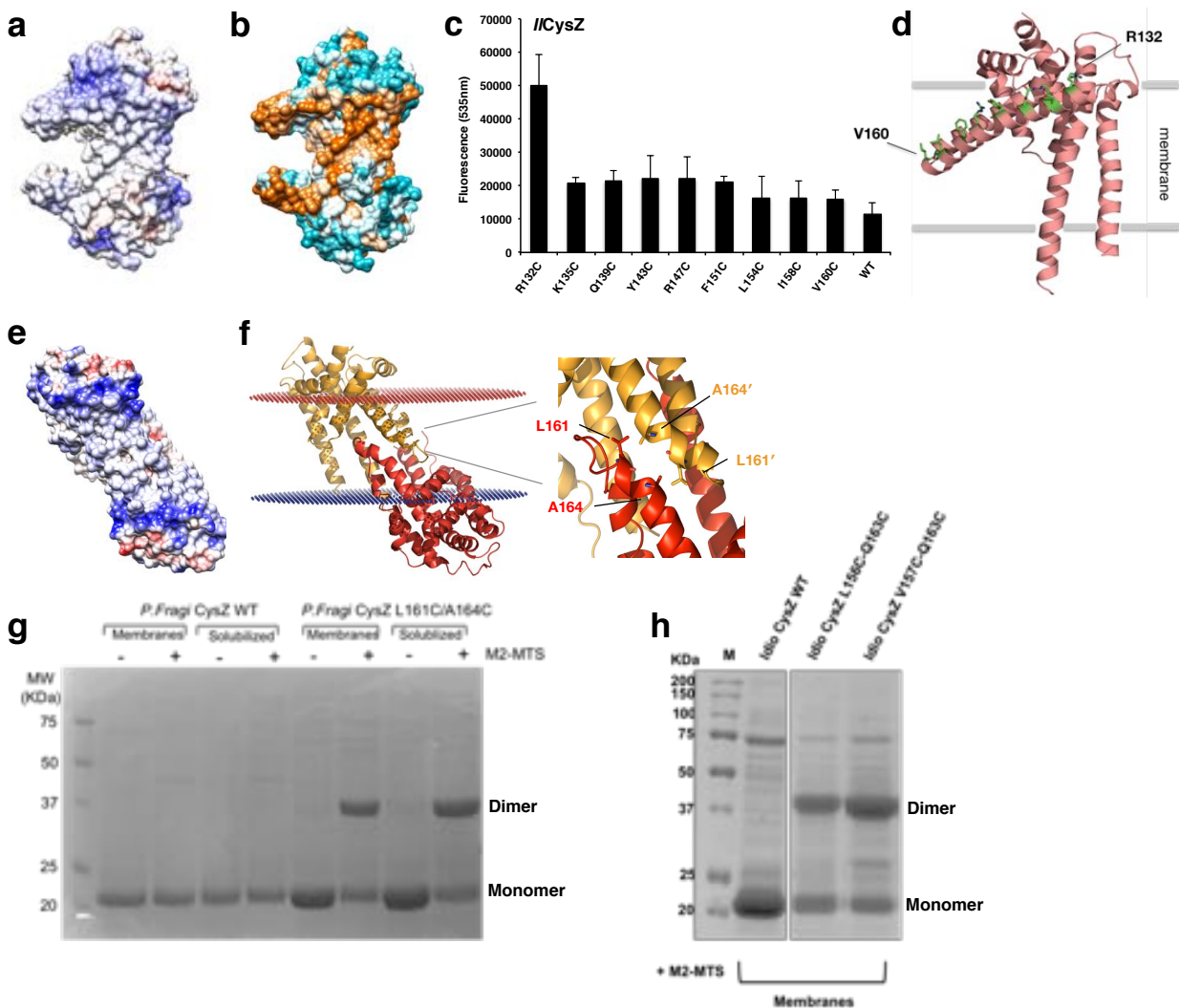
837

838

839 **Fig. 3. S2. Surface electrostatics, hydrophobicity and site-directed fluorescence labeling of**

840 **cysteine mutants located on H4 of *Il*CysZ.** a. A depiction of the surface electrostatic potentials

841 of the *Il*CysZ dimer with negative surface potential represented in red, and positive potential in

842 blue as calculated by APBS. b. Surface of *Il*CysZ rendered by level of hydrophicity, using the

843 Kyte-Doolitle hydrophobicity scale with cyan being most polar, to orange being most

844 hydrophobic, reveals a hydrophobic belt along the center of the dimer, suggesting the orientation

845 of the dimer in the lipid bilayer. c, d. Single cysteine mutants were designed to be located along

44

846 the length of helix 4 of CysZ, to gauge the extent of its membrane insertion. The labeled protein

847 was extracted from the membrane and purified after quenching the labeling reaction.

848 Fluorescence intensity was measured and quantified by a Tecan fluorescence plate reader at an

849 excitation of 485nm and emission of 535nm the results of which were plotted on the left, with

850 error bars representing the standard deviation from the mean for n=3. The results show that of all

851 the residues on the helix, only R132C (the top-most residue) was accessible to the fluorophore

852 and hence exposed out of the membrane. d. Locations of the mutated residues on helix H4 are

853 marked on the model of *Il*CysZ in green. Crosslinking of L161C-A164C cysteine mutant of

854 *Pf*CysZ and *Il*CysZ exhibits dimer formation. e. A depiction of the surface electrostatic

855 potentials of the *Pf*CysZ dimer with negative surface potential represented in red, and positive

856 potential in blue as calculated by APBS, highlights hydrophobic belt marking the orientation of

857 the *Pf*CysZ dimer in the membrane. f. Membrane orientation of *Pf*CysZ predicted by OPM/PPM

858 server shows its 31-degree tilt to the perpendicular, with a zoomed in view of the location of the

859 cysteine mutants at the dimer interface, used for crosslinking of the dimer. g. h. Dimer formation

860 by the crosslinking of *Pf*CysZ (g) and *Il*CysZ (h) with introduced structure-based cysteine

861 substitution mutations in the H4-H5 dimer interface. Analogous pairs of cysteine mutants from

862 each species are shown here: *Pf*CysZ L161C-A164C and *Il*CysZ L156C-Q163C and V157C-

863 Q163C. Sulfydryl specific Bis-MTS crosslinkers of a certain spacer length (in this case 5.2Å)

864 were used at 0.5mM for 1hour at room temperature to crosslink the protein. Experiment was

865 performed on protein in the membrane, as well as on solubilized protein. WT protein (cysteine-

866 less) was used as a control. Proteins were purified after stopping the reaction, and run on an SDS

867 PAGE with reducing dye, and stained with Coomassie blue.

868

869   **Figure 4.**

870
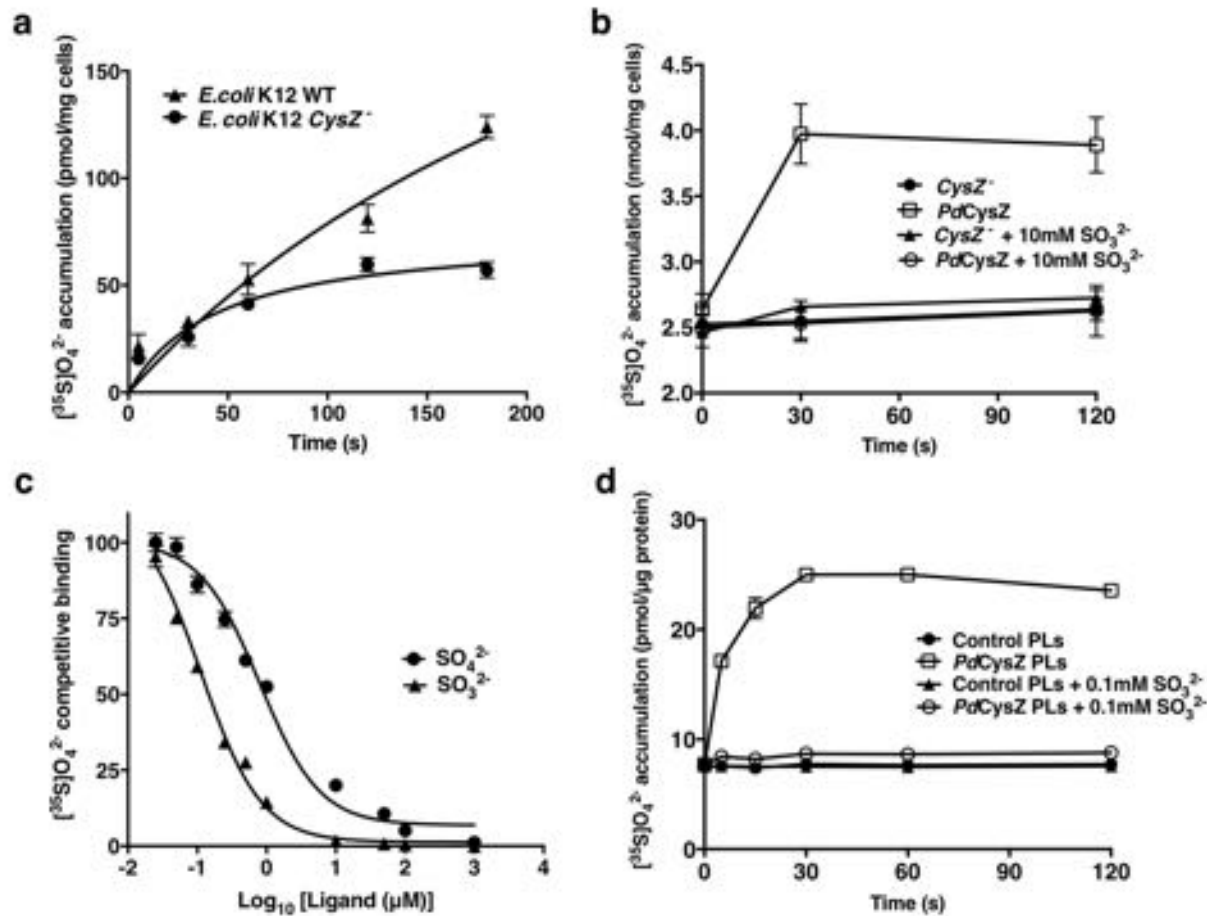
871

872

873   **Fig. 4. Functional characterization of CysZ.** a. Time course of $[^{35}S]O_4^{2-}$ uptake (320 μM) by

874   cells of WT *E. coli K12* (strain BW25113) and by CysZ$^-$ (strain JW2406-1) cells (n=3). b. Sulfite

875   inhibition of sulfate uptake. Radiolabeled sulfate (320 μM $[^{35}S]O_4^{2-}$) uptake is rescued in the

876   same *cysZ* knockout strain by transformation with an expression vector for *Pd*CysZ whereas the

877   control cells were transformed with an empty vector. Sulfate uptake is inhibited by the addition

878   of 10 mM SO_3^{2-} (n=3). c. Competitive binding of labeled sulfate in presence of unlabeled

879   ligands. The inhibition of labeled sulfate (7 nM $[^{35}S]O_4^{2-}$) binding by non-labeled sulfate or

46

880   sulfite is measured by the scintillation proximity assay using purified $PdCysZ$ (n=3). $PdCysZ$

881   binds SO_4^{2-} with an EC_{50} of 0.81 ± 0.045 μM and exhibits an IC_{50} of 0.12 ± 0.034 μM for SO_3^{-2}.

882   d. Radiolabeled sulfate (10 μM [^{35}S]O_4^{2-}) accumulation into proteoliposomes reconstituted with

883   detergent-purified $PdCysZ$. Uptake into reconstituted proteoliposomes (open squares) is shown

884   in comparison with control (empty) liposomes (solid discs). Uptake is inhibited by the presence

885   of 0.1 mM SO_3^{2-} (n=3).

886

887   **Figure 4 – Figure Supplement 1.**

888
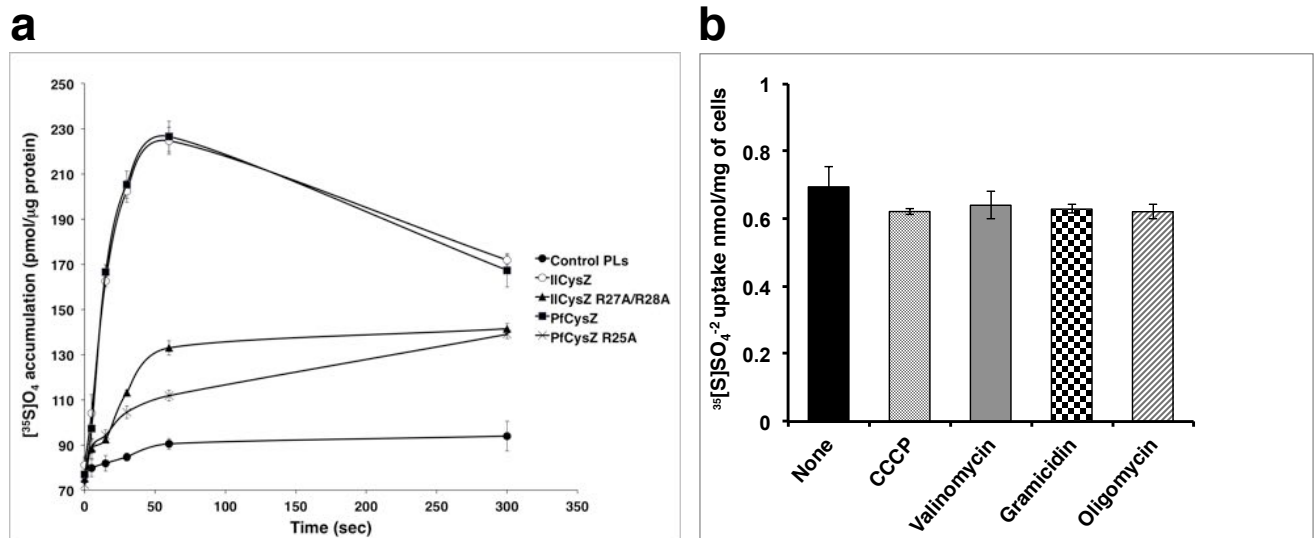
889

890

891   **Fig. 4. S1. a. Radiolabeled sulfate (10 μM [^{35}S]O$_4^{2-}$) accumulation is measured from**

892   **detergent purified *Il*CysZ and *Pf*CysZ reconstituted in proteoliposomes, in comparison to**

893   **the control (empty) liposomes.** Sulfate-binding site alanine mutants (*Il*CysZ R27A/R28A and

894   *Pf*CysZ R25A) display a significantly diminished sulfate uptake capability. Error bars represent

895   the standard deviation from the mean (SEM), for n=3. b. Effect of uncouplers and ionophores on

896   the sulfate accumulation by CysZ. *Il*CysZ expressed in the *E. coli* knockout strain shows

897   unchanged sulfate uptake levels in the presence of the uncouplers CCCP and oligomycin or the

898   ionophores gramicidin and valinomycin. Sulfate accumulation was measured in triplicate at pH 7

899   and total accumulation was plotted after a 10 s incubation. Error bars were calculated by standard

900   deviation from the mean, for n=3.

901

902 **Figure 4 – Figure Supplement 2.**
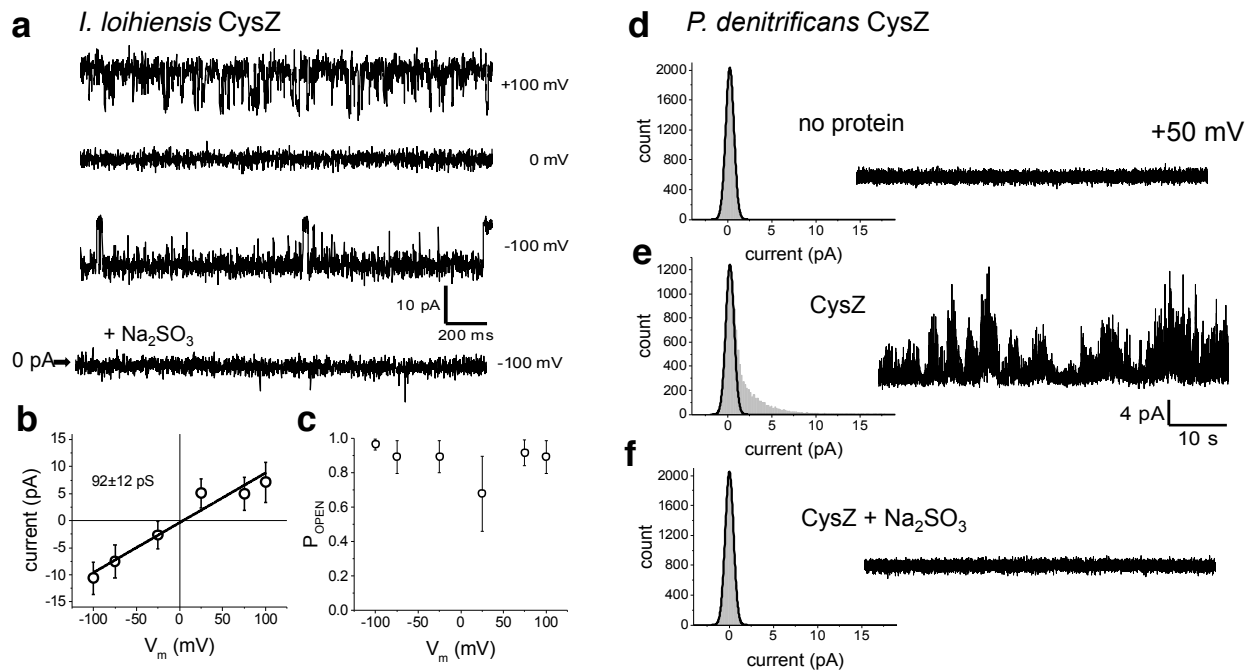
903

904

905 **Fig. 4. S2.** **Reconstitution of CysZ in planar lipid bilayers yields sulfite-sensitive**

906 **conductances.** a. Sample traces of *Il*CysZ under 150 mM symmetrical Na_2SO_4 solutions at the

907 indicated membrane potentials and pH = 5.4. The lowest trace shows inhibition of activity by 15

908 μM Na_2SO_3. b. Unitary conductance estimated at 92 ± 12 pS with a reversal potential (E_{rev}) at 0

909 mV. c. Unitary open probability does not change as a function of membrane potential, and is

910 stable at an average $P_{OPEN} = 0.8$. d. Stable bilayer recording at a membrane potential $V_m = +50$

911 mV, with no protein reconstituted. An all point current amplitude histogram is plotted on the left

912 of the trace. The peak of the normal distribution denotes the baseline zero current. e.

913 Reconstitution of *Pd*CysZ under 150 mM symmetrical Na_2SO_4 solutions at +50 mV. An all point

914 current amplitude histogram is plotted on the left of the trace. The high frequency activity shows

915 a poorly resolved distribution of unitary currents above baseline. f. Inhibition of activity by 5 μM

49

916   Na$_2$SO$_3$. An all point current amplitude histogram is plotted on the left of the trace. Sulfite

917   inhibited activity back to baseline levels.

918

919   **Figure 5.**
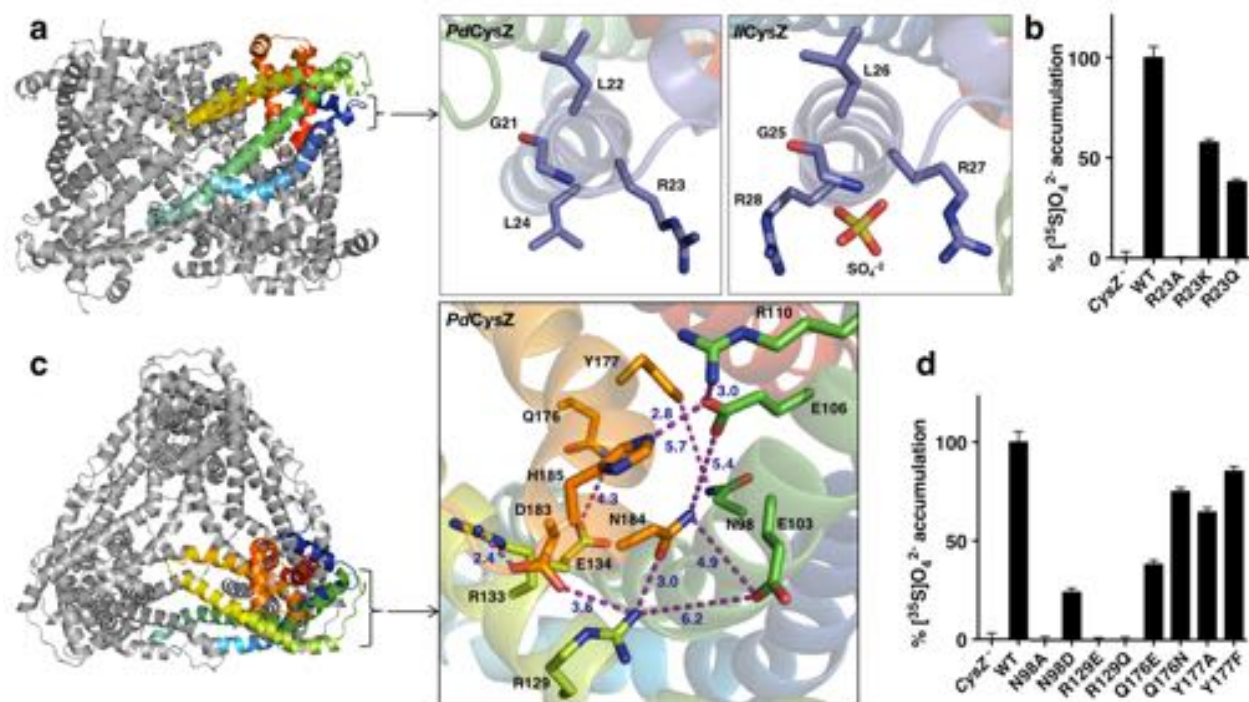
920

921

922   **Fig. 5. Functionally relevant features of the CysZ molecule** a. Side-view of a ribbon diagram

923   of the *Pd*CysZ hexamer, with one chain rainbow-colored from N- (blue) to C-termini (red).

924   Insets show the sulfate-binding site located at the start of H2a in *Pd*CysZ (left), with conserved

925   residues G21, L22, R23 and L24 labeled, and the corresponding site in *Il*CysZ (right), with

926   residues G25, L26, R27, and R28 labeled and showing the SO_4^{-2} ion as bound in the crystal

927   structure. b. Sulfate uptake by sulfate-binding site mutants of *Pd*CysZ. *E. coli K12* CysZ⁻ cells

928   transformed with the listed *Pd*CysZ R23 mutants were used to measure $[^{35}S]O_4^{-2}$ uptake (n=3).

929   Sulfate uptake was abolished for R23A, and rescued to 50% and 40% of the wild type levels for

930   the R23K and R23Q mutants respectively. c. A top-view of the *Pd*CysZ hexamer, colored as in a.

931   The inset magnifies the central core of CysZ to show the associated network of hydrogen bonds

932   (R129-N184, E106-H185), van der Waals interactions (E103-N184, E106-N184, Q176-E134)

51

933   and salt bridges (R129-D183, R133-D183, R110-E106) between pairs of highly conserved

934   residues. Interatomic contacts are shown as purple dotted lines with distances (in Å) marked in

935   blue. d. Sulfate uptake by central-core mutants of *Pd*CysZ. *E. coli K12* CysZ⁻ cells transformed

936   with the listed *Pd*CysZ mutants were used to measure $[^{35}S]O_4^{-2}$ uptake (n=3). N98A and R129E

937   and R129Q showed severely impaired sulfate uptake, whereas more conservative substitutions

938   such as N98D, Q176E and Q176N had less of a negative effect on function. Y177A and Y177F

939   do not show any impaired function.

940

941 **Figure 6.**
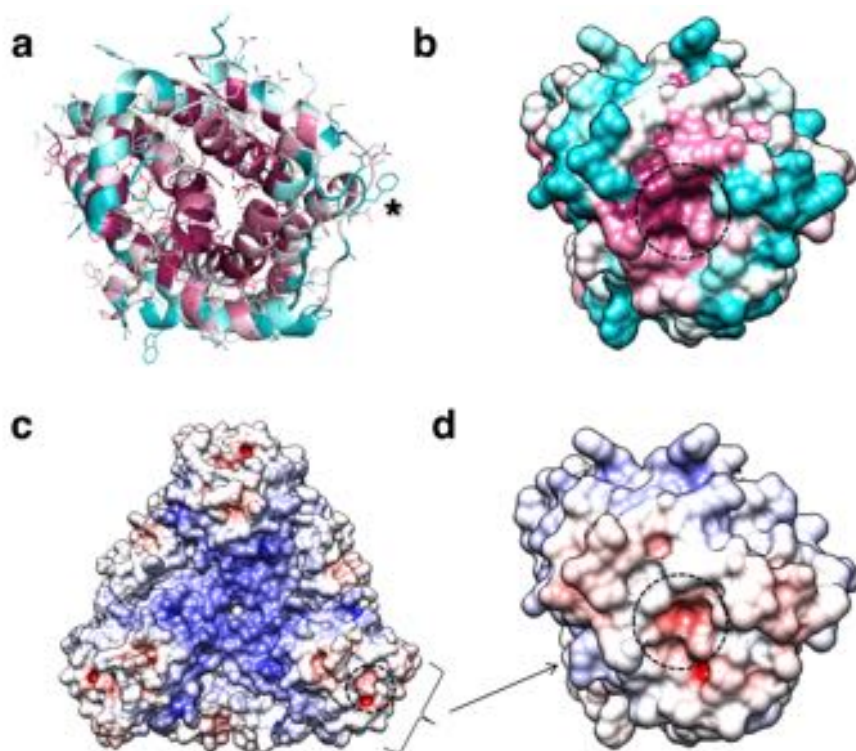
942

943

944 **Fig. 6. Conservation and entrance of putative pore of *Pd*CysZ.** a. Ribbon diagram colored by

945 conservation with residues in maroon being most conserved to cyan being least conserved

946 (calculated by ConSurf) to highlight the entrance to the putative pore; an asterisk (*) marks the

947 location of the sulfate-binding site (GLR motif) at top of H2a. b. Same view and coloring scheme

948 as in a, but now shown in surface representation. c. Electrostatic representation of hexameric

949 *Pd*CysZ as viewed from the top, with negative surface potential represented in red, and positive

950 potential in blue as calculated by APBS, with location of the putative pore marked by a dashed

951 circle. d. Close-up view in electrostatic representation of the putative pore within a *Pd*CysZ

952 protomer, surface and orientation as in b.

953

954 **Figure 7.**
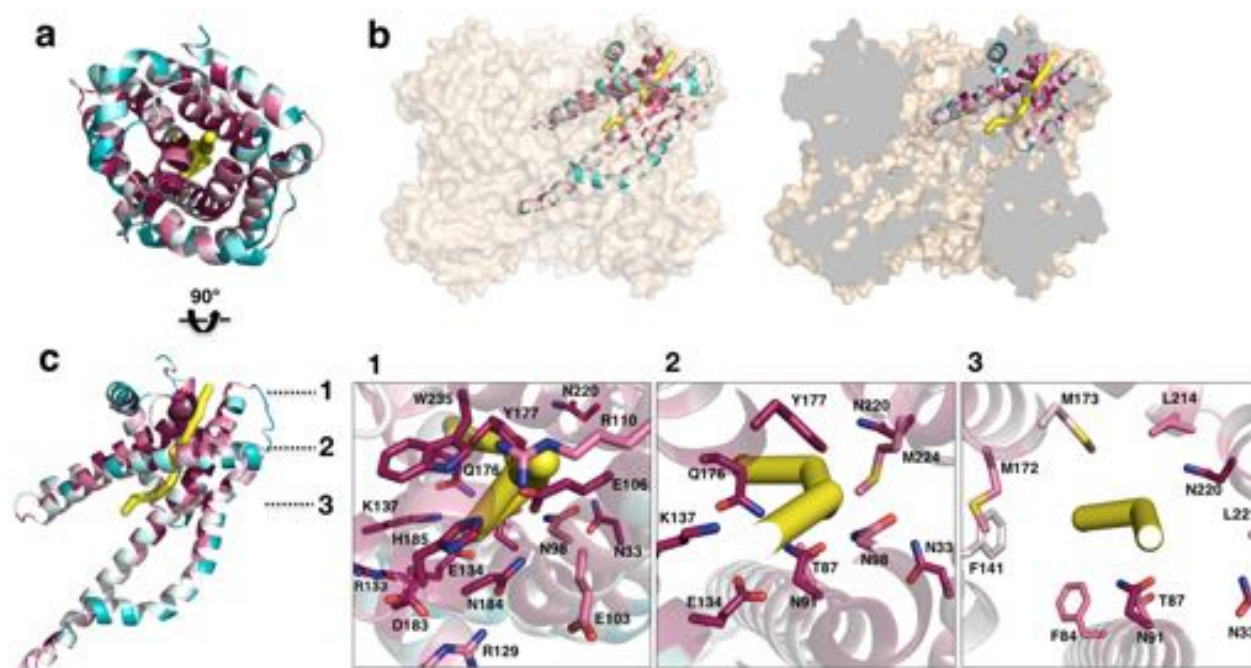
955

956

957 **Fig. 7. Putative ion conductance pathway of CysZ.** a. A *Pd*CysZ protomer looking into the

958 incipient pore entrance. The polypeptide ribbon is oriented as in 6a and colored by level of

959 sequence conservation (calculated by ConSurf, with maroon being most conserved and cyan

960 least). The putative pore and ion conduction pathway is shown as a yellow tube of 1 Å diameter,

961 calculated by PoreWalker. b. Surface representation of the *Pd*CysZ hexamer, as side views, both

962 semi-transparent (left) and with surface clipped (right, cut surfaces colored in grey) to allow for

963 the internal visualization of the pathway leading to the central cavity. c. Side view of a *Pd*CysZ

964 protomer left, viewed as in b and rotated 90° from a. Insets show magnified views of cross-

965 sections along the pathway: At level 1, the entrance to the pore consists of a narrow constriction

966 created by a network of highly conserved polar and charged residues (E106, R110, E134, N184,

967 H185) tightly interacting with one another. At level 2, the pathway broadens and becomes less

968   charged, but yet polar in nature as lined by conserved asparagine, tyrosine and threonine residues

969   (N33, T87, N91, N98, Q176, Y177). From level 3, the pathway widens further and ultimately

970   leads into the large central hydrophobic cavity.

971

972   **Figure 7 – Figure Supplement 1.**

973
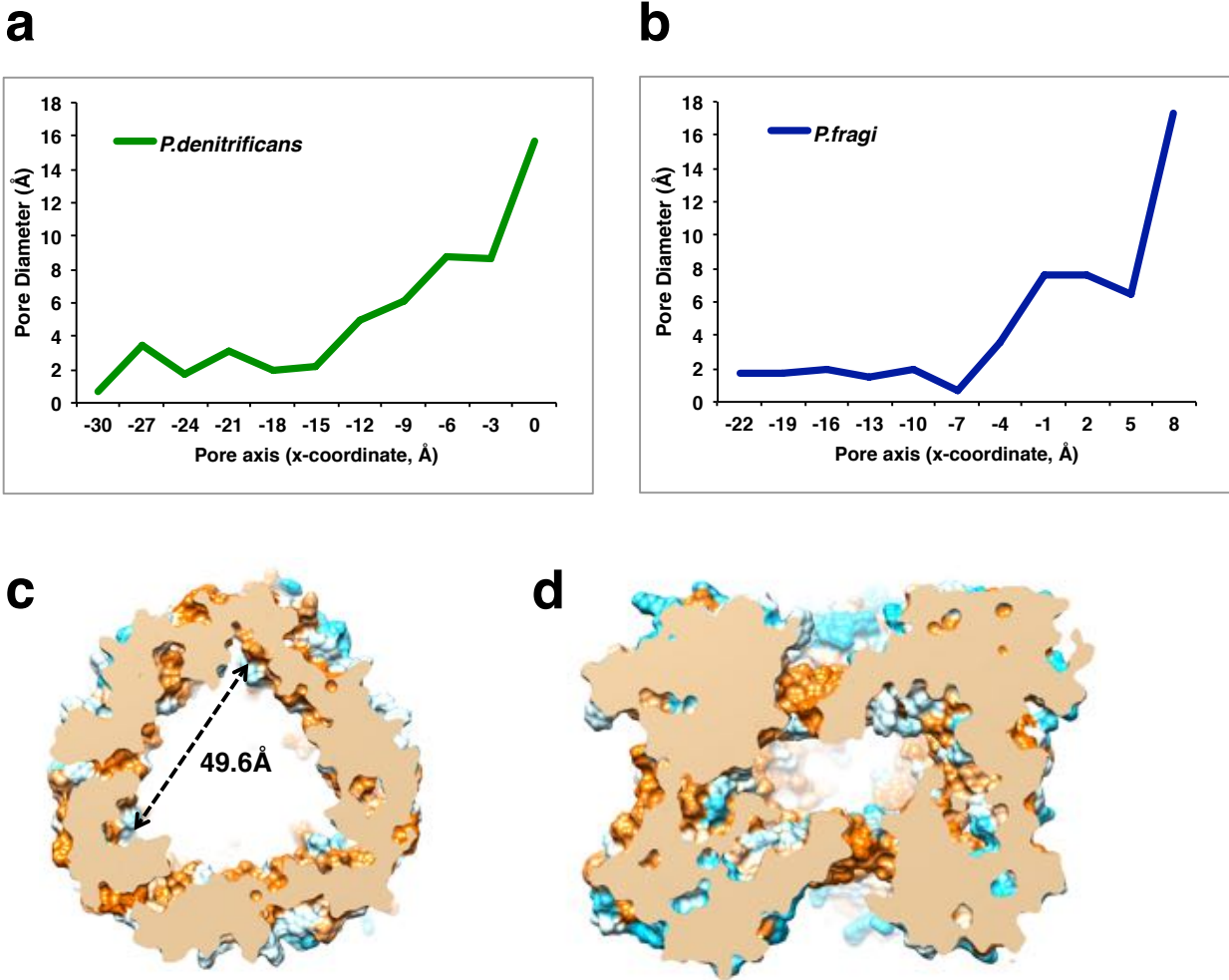
974
975

976   **Fig. 7. S1. Plot of the pore diameter of the putative ion conduction pathway.** a. *Pd*CysZ b.

977   *Pf*CysZ, showing a very narrow constriction of under 2 Å in diameter near the entrance of the

978   pore, which then widens as the ions move past the core of the protomer to the inner central cavity

979   of the hexameric channel (as calculated by PoreWalker, measured at 3 Å steps along the x-axis)

980   c. Central hydrophobic cavity of *Pd*CysZ hexamer, cross-section of central cavity of the

981   hexameric *Pd*CysZ (top view) and d. side view, shows a triangular-shaped cavity with each side

982   measuring 49.6 Å in length. The cavity is primarily hydrophobic, as depicted and colored with

983   the Kyte-Doolitle hydrophobicity scale from most polar colored in cyan to most hydrophobic

984   colored in orange.

985

References:

Adams, P. D., Afonine, P. V., Bunkoczi, G., Chen, V. B., Davis, I. W., Echols, N., Headd, J. J., Hung, L. W., Kapral, G. J., Grosse-Kunstleve, R. W., McCoy, A. J., Moriarty, N. W., Oeffner, R., Read, R. J., Richardson, D. C., Richardson, J. S., Terwilliger, T. C., & Zwart, P. H. (2010). PHENIX: a comprehensive Python-based system for macromolecular structure solution. *Acta Crystallogr D Biol Crystallogr, 66*(Pt 2), 213-221. doi:S0907444909052925 [pii] 10.1107/S0907444909052925

Aguilar-Barajas, E., Diaz-Perez, C., Ramirez-Diaz, M. I., Riveros-Rosas, H., & Cervantes, C. (2011). Bacterial transport of sulfate, molybdate, and related oxyanions. *Biometals, 24*(4), 687-707. doi:10.1007/s10534-011-9421-x

Akabas, M. H., Stauffer, D. A., Xu, M., & Karlin, A. (1992). Acetylcholine receptor channel structure probed in cysteine-substitution mutants. *Science, 258*(5080), 307-310.

Amadi, S. T., Koteiche, H. A., Mishra, S., & McHaourab, H. S. (2010). Structure, dynamics, and substrate-induced conformational changes of the multidrug transporter EmrE in liposomes. *J Biol Chem, 285*(34), 26710-26718. doi:10.1074/jbc.M110.132621

Anishkin, A., Akitake, B., Kamaraju, K., Chiang, C. S., & Sukharev, S. (2010). Hydration properties of mechanosensitive channel pores define the energetics of gating. *J Phys Condens Matter, 22*(45), 454120. doi:10.1088/0953-8984/22/45/454120

Aryal, P., Sansom, M. S., & Tucker, S. J. (2015). Hydrophobic Gating in Ion Channels. *Journal of Molecular Biology, 427*(1), 121-130. doi:10.1016/j.jmb.2014.07.030

Ashkenazy, H., Abadi, S., Martz, E., Chay, O., Mayrose, I., Pupko, T., & Ben-Tal, N. (2016). ConSurf 2016: an improved methodology to estimate and visualize evolutionary conservation in macromolecules. *Nucleic Acids Res, 44*(W1), W344-350. doi:10.1093/nar/gkw408

Aslanidis, C., & de Jong, P. J. (1990). Ligation-independent cloning of PCR products (LIC-PCR). *Nucleic Acids Res, 18*(20), 6069-6074.

Baba, T., Ara, T., Hasegawa, M., Takai, Y., Okumura, Y., Baba, M., Datsenko, K. A., Tomita, M., Wanner, B. L., & Mori, H. (2006). Construction of Escherichia coli K-12 in-frame, single-gene knockout mutants: the Keio collection. *Mol Syst Biol, 2*, 2006 0008. doi:10.1038/msb4100050

Barton, L. L. (2005) *Structural and Functional Relationships in Prokaryotes* (pp. 680-720): Springer.

Bass, R. B., Strop, P., Barclay, M., & Rees, D. C. (2002). Crystal structure of Escherichia coli MscS, a voltage-modulated and mechanosensitive channel. *Science, 298*(5598), 1582-1587. doi:10.1126/science.1077945

Birkner, J. P., Poolman, B., & Kocer, A. (2012). Hydrophobic gating of mechanosensitive channel of large conductance evidenced by single-subunit resolution. *Proc Natl Acad Sci U S A, 109*(32), 12944-12949. doi:10.1073/pnas.1205270109

Britton, P., Boronat, A., Hartley, D. A., Jones-Mortimer, M. C., Kornberg, H. L., & Parra, F. (1983). Phosphotransferase-mediated regulation of carbohydrate utilization in Escherichia coli K12: location of the gsr (tgs) and iex (crr) genes by specialized transduction. *J Gen Microbiol, 129*(2), 349-356.

1030   Buckler, K. J., & Vaughan-Jones, R. D. (1998). Effects of mitochondrial uncouplers on
1031   intracellular calcium, pH and membrane potential in rat carotid body type I cells. *J*
1032   *Physiol, 513 (Pt 3)*, 819-833.
1033   Chen, Y. H., Hu, L., Punta, M., Bruni, R., Hillerich, B., Kloss, B., Rost, B., Love, J.,
1034   Siegelbaum, S. A., & Hendrickson, W. A. (2010). Homologue structure of the SLAC1
1035   anion channel for closing stomata in leaves. *Nature, 467*(7319), 1074-1080.
1036   doi:10.1038/nature09487
1037   nature09487 [pii]
1038   Cowtan, K. D., & Zhang, K. Y. (1999). Density modification for macromolecular phase
1039   improvement. *Prog Biophys Mol Biol, 72*(3), 245-270.
1040   Czodrowski, P., Dramburg, I., Sotriffer, C. A., & Klebe, G. (2006). Development, validation, and
1041   application of adapted PEOE charges to estimate pKa values of functional groups in
1042   protein-ligand complexes. *Proteins, 65*(2), 424-437. doi:10.1002/prot.21110
1043   Davis, B. D., & Mingioli, E. S. (1950). Mutants of Escherichia coli requiring methionine or
1044   vitamin B12. *J Bacteriol, 60*(1), 17-28.
1045   Dolinsky, T. J., Czodrowski, P., Li, H., Nielsen, J. E., Jensen, J. H., Klebe, G., & Baker, N. A.
1046   (2007). PDB2PQR: expanding and upgrading automated preparation of biomolecular
1047   structures for molecular simulations. *Nucleic Acids Res, 35*(Web Server issue), W522-
1048   525. doi:10.1093/nar/gkm276
1049   Dolinsky, T. J., Nielsen, J. E., McCammon, J. A., & Baker, N. A. (2004). PDB2PQR: an
1050   automated pipeline for the setup of Poisson-Boltzmann electrostatics calculations.
1051   *Nucleic Acids Res, 32*(Web Server issue), W665-667. doi:10.1093/nar/gkh381
1052   Doyle, D. A., Morais Cabral, J., Pfuetzner, R. A., Kuo, A., Gulbis, J. M., Cohen, S. L., Chait, B.
1053   T., & MacKinnon, R. (1998). The structure of the potassium channel: molecular basis of
1054   K+ conduction and selectivity. *Science, 280*(5360), 69-77.
1055   Emsley, P., Lohkamp, B., Scott, W. G., & Cowtan, K. (2010). Features and development of
1056   Coot. *Acta Crystallogr D Biol Crystallogr, 66*(Pt 4), 486-501. doi:S0907444910007493
1057   [pii]
1058   10.1107/S0907444910007493
1059   Evans, P. (2006). Scaling and assessment of data quality. *Acta Crystallogr D Biol Crystallogr,*
1060   *62*(Pt 1), 72-82. doi:10.1107/S0907444905036693
1061   Glaser, F., Pupko, T., Paz, I., Bell, R. E., Bechor-Shental, D., Martz, E., & Ben-Tal, N. (2003).
1062   ConSurf: identification of functional regions in proteins by surface-mapping of
1063   phylogenetic information. *Bioinformatics, 19*(1), 163-164.
1064   Hanahan, D. (1983). Studies on transformation of Escherichia coli with plasmids. *Journal of*
1065   *Molecular Biology, 166*(4), 557-580.
1066   Hryniewicz, M., Sirko, A., Palucha, A., Bock, A., & Hulanicka, D. (1990). Sulfate and
1067   thiosulfate transport in Escherichia coli K-12: identification of a gene encoding a novel
1068   protein involved in thiosulfate binding. *J Bacteriol, 172*(6), 3358-3366.
1069   Kabsch, W. (2010). Xds. *Acta Crystallogr D Biol Crystallogr, 66*(Pt 2), 125-132.
1070   doi:10.1107/S0907444909047337
1071   Kertesz, M. A. (2000). Riding the sulfur cycle--metabolism of sulfonates and sulfate esters in
1072   gram-negative bacteria. *FEMS Microbiol Rev, 24*(2), 135-175.
1073   Kertesz, M. A. (2001). Bacterial transporters for sulfate and organosulfur compounds. *Res*
1074   *Microbiol, 152*(3-4), 279-290.

1075 Korkhov, V. M., & Tate, C. G. (2009). An emerging consensus for the structure of EmrE. *Acta*
1076   *Crystallogr D Biol Crystallogr, 65*(Pt 2), 186-192. doi:10.1107/S0907444908036640
1077 Kredich, N. M. (1971). Regulation of L-cysteine biosynthesis in Salmonella typhimurium. I.
1078   Effects of growth of varying sulfur sources and O-acetyl-L-serine on gene expression. *J*
1079   *Biol Chem, 246*(11), 3474-3484.
1080 Kredich, N. M., Hulanicka, M. D., & Hallquist, S. G. (1979). Synthesis of L-cysteine in
1081   Salmonella typhimurium. *Ciba Found Symp*(72), 87-99.
1082 Krissinel, E., & Henrick, K. (2007). Inference of macromolecular assemblies from crystalline
1083   state. *Journal of Molecular Biology, 372*(3), 774-797 'Protein interfaces, surfaces and
1084   assemblies' service PISA at the European Bioinformatics Institute.
1085   (http://www.ebi.ac.uk/pdbe/prot_int/pistart.html). doi:10.1016/j.jmb.2007.05.022
1086 Langer, G., Cohen, S. X., Lamzin, V. S., & Perrakis, A. (2008). Automated macromolecular
1087   model building for X-ray crystallography using ARP/wARP version 7. *Nat Protoc, 3*(7),
1088   1171-1179. doi:nprot.2008.91 [pii]
1089 10.1038/nprot.2008.91
1090 Leal-Pinto, E., London, R. D., Knorr, B. A., & Abramson, R. G. (1995). Reconstitution of
1091   hepatic uricase in planar lipid bilayer reveals a functional organic anion channel. *J*
1092   *Membr Biol, 146*(2), 123-132.
1093 Liu, Q., Dahmane, T., Zhang, Z., Assur, Z., Brasch, J., Shapiro, L., Mancia, F., & Hendrickson,
1094   W. A. (2012). Structures from anomalous diffraction of native biological
1095   macromolecules. *Science, 336*(6084), 1033-1037. doi:10.1126/science.1218753
1096 Liu, Q., Zhang, Z., & Hendrickson, W. A. (2011). Multi-crystal anomalous diffraction for low-
1097   resolution macromolecular phasing. *Acta Crystallogr D Biol Crystallogr, 67*(Pt 1), 45-59.
1098   doi:10.1107/S0907444910046573
1099 Lomize, M. A., Pogozheva, I. D., Joo, H., Mosberg, H. I., & Lomize, A. L. (2012). OPM
1100   database and PPM web server: resources for positioning of proteins in membranes.
1101   *Nucleic Acids Res, 40*(Database issue), D370-376. doi:10.1093/nar/gkr703
1102 Loughlin, P., Shelden, M. C., Tierney, M. L., & Howitt, S. M. (2002). Structure and function of a
1103   model member of the SulP transporter family. *Cell Biochem Biophys, 36*(2-3), 183-190.
1104   doi:CBB:36:2-3:183 [pii]
1105 10.1385/CBB:36:2-3:183
1106 Love, J., Mancia, F., Shapiro, L., Punta, M., Rost, B., Girvin, M., Wang, D. N., Zhou, M., Hunt,
1107   J. F., Szyperski, T., Gouaux, E., MacKinnon, R., McDermott, A., Honig, B., Inouye, M.,
1108   Montelione, G., & Hendrickson, W. A. (2010). The New York Consortium on Membrane
1109   Protein Structure (NYCOMPS): a high-throughput platform for structural genomics of
1110   integral membrane proteins. *J Struct Funct Genomics, 11*(3), 191-199.
1111   doi:10.1007/s10969-010-9094-7
1112 Mancia, F., & Love, J. (2011). High throughput platforms for structural genomics of integral
1113   membrane proteins. *Curr Opin Struct Biol, 21*(4), 517-522. doi:10.1016/j.sbi.2011.07.001
1114 Mansilla, M. C., & de Mendoza, D. (2000). The Bacillus subtilis cysP gene encodes a novel
1115   sulphate permease related to the inorganic phosphate transporter (Pit) family.
1116   *Microbiology, 146 (Pt 4)*, 815-821.
1117 McCoy, A. J., Grosse-Kunstleve, R. W., Adams, P. D., Winn, M. D., Storoni, L. C., & Read, R.
1118   J. (2007). Phaser crystallographic software. *Journal of Applied Crystallography, 40*(Pt 4),
1119   658-674. doi:10.1107/S0021889807021206

Morera, F. J., Vargas, G., Gonzalez, C., Rosenmann, E., & Latorre, R. (2007). Ion-channel reconstitution. *Methods Mol Biol, 400*, 571-585. doi:10.1007/978-1-59745-519-0_38

Mueller, P., Rudin, D. O., Tien, H. T., & Wescott, W. C. (1962). Reconstitution of cell membrane structure in vitro and its transformation into an excitable system. *Nature, 194*, 979-980.

Otwinowski, Z., & Minor, W. (1997). Processing of X-ray Diffraction Data Collected in Oscillation Mode. *Methods in Enzymology, 276*, 307-326.

Pape, T., & Schneider, T. R. (2004). HKL2MAP: a graphical user interface for macromolecular phasing with SHELX programs. *J. Appl. Cryst., 37*, 843-844.

Parra, F., Britton, P., Castle, C., Jones-Mortimer, M. C., & Kornberg, H. L. (1983). Two separate genes involved in sulphate transport in Escherichia coli K12. *J Gen Microbiol, 129*(2), 357-358.

Pellegrini-Calace, M., Maiwald, T., & Thornton, J. M. (2009). PoreWalker: a novel tool for the identification and characterization of channels in transmembrane proteins from their three-dimensional structure. *PLoS Comput Biol, 5*(7), e1000440. doi:10.1371/journal.pcbi.1000440

Pettersen, E. F., Goddard, T. D., Huang, C. C., Couch, G. S., Greenblatt, D. M., Meng, E. C., & Ferrin, T. E. (2004). UCSF Chimera--a visualization system for exploratory research and analysis. *J Comput Chem, 25*(13), 1605-1612. doi:10.1002/jcc.20084

Punta, M., Love, J., Handelman, S., Hunt, J. F., Shapiro, L., Hendrickson, W. A., & Rost, B. (2009). Structural genomics target selection for the New York consortium on membrane protein structure. *J Struct Funct Genomics, 10*(4), 255-268. doi:10.1007/s10969-009-9071-1

Quick, M., & Javitch, J. A. (2007). Monitoring the function of membrane transport proteins in detergent-solubilized form. *Proc Natl Acad Sci U S A, 104*(9), 3603-3608. doi:0609573104 [pii]
10.1073/pnas.0609573104

Rapp, M., Granseth, E., Seppala, S., & von Heijne, G. (2006). Identification and evolution of dual-topology membrane proteins. *Nat Struct Mol Biol, 13*(2), 112-116. doi:10.1038/nsmb1057

Rigaud, J. L., Pitard, B., & Levy, D. (1995). Reconstitution of membrane proteins into liposomes: application to energy-transducing membrane proteins. *Biochim Biophys Acta, 1231*(3), 223-246.

Schrodinger, LLC. (2010). *The PyMOL Molecular Graphics System, Version 1.3r1*.

Sheldrick, G. M. (2010). Experimental phasing with SHELXC/D/E: combining chain tracing with density modification. *Acta Crystallogr D Biol Crystallogr, 66*(Pt 4), 479-485. doi:S0907444909038360 [pii]
10.1107/S0907444909038360

Sirko, A., Zatyka, M., Sadowy, E., & Hulanicka, D. (1995). Sulfate and thiosulfate transport in Escherichia coli K-12: evidence for a functional overlapping of sulfate- and thiosulfate-binding proteins. *J Bacteriol, 177*(14), 4134-4136.

Stein, N. (2008). CHAINSAW: a program for mutating pdb files used as templates in molecular replacement. *Journal of Applied Crystallography, 41*, 641-643. doi:10.1107/S0021889808006985

1164   Stockbridge, R. B., Kolmakova-Partensky, L., Shane, T., Koide, A., Koide, S., Miller, C., &
1165   Newstead, S. (2015). Crystal structures of a double-barrelled fluoride ion channel.
1166   *Nature, 525*(7570), 548-551. doi:10.1038/nature14981
1167   Stockbridge, R. B., Robertson, J. L., Kolmakova-Partensky, L., & Miller, C. (2013). A family of
1168   fluoride-specific ion channels with dual-topology architecture. *Elife, 2*, e01084.
1169   doi:10.7554/eLife.01084
1170   Winn, M. D., Ballard, C. C., Cowtan, K. D., Dodson, E. J., Emsley, P., Evans, P. R., Keegan, R.
1171   M., Krissinel, E. B., Leslie, A. G., McCoy, A., McNicholas, S. J., Murshudov, G. N.,
1172   Pannu, N. S., Potterton, E. A., Powell, H. R., Read, R. J., Vagin, A., & Wilson, K. S.
1173   (2011). Overview of the CCP4 suite and current developments. *Acta Crystallogr D Biol
1174   Crystallogr, 67*(Pt 4), 235-242. doi:10.1107/S0907444910045749
1175   Yang, T., Liu, Q., Kloss, B., Bruni, R., Kalathur, R. C., Guo, Y., Kloppmann, E., Rost, B.,
1176   Colecraft, H. M., & Hendrickson, W. A. (2014). Structure and selectivity in bestrophin
1177   ion channels. *Science, 346*(6207), 355-359. doi:10.1126/science.1259723
1178   Ye, L., Jia, Z., Jung, T., & Maloney, P. C. (2001). Topology of OxlT, the oxalate transporter of
1179   Oxalobacter formigenes, determined by site-directed fluorescence labeling. *J Bacteriol,
1180   183*(8), 2490-2496. doi:10.1128/JB.183.8.2490-2496.2001
1181   Zhang, L., Jiang, W., Nan, J., Almqvist, J., & Huang, Y. (2014). The Escherichia coli CysZ is a
1182   pH dependent sulfate transporter that can be inhibited by sulfite. *Biochim Biophys Acta,
1183   1838*(7), 1809-1816. doi:10.1016/j.bbamem.2014.03.003
1184